

Tectonics°

RESEARCH ARTICLE

10.1029/2024TC008308

Key Points:

- Integrating flexural- and thermalkinematic models with thermochronology data provides constraints on crustal-scale normal fault evolution
- Results show how effective elastic thickness, fault geometry, and detachment depth impact fault evolution and predicted age data
- For the contested displacement history
 of the Teton fault example, analyses
 indicate >11 km and potentially
 >16 km of normal displacement

Supporting Information:

Supporting Information may be found in the online version of this article.

Correspondence to:

J. R. Thigpen, ryan.thigpen@uky.edu

Citation

Helfrich, A. L., Thigpen, J. R., Buford-Parks, V. M., McQuarrie, N., Brown, S. J., & Goldsby, R. C. (2024). Constraining displacement magnitude on crustal-scale extensional faults using thermochronology combined with flexural-kinematic and thermal-kinematic modeling: An example from the Teton fault, Wyoming, USA. *Tectonics*, 43, e2024TC008308. https://doi.org/10.1029/2024TC008308

Received 26 FEB 2024 Accepted 23 JUN 2024

Author Contributions:

Conceptualization: Autumn L. Helfrich, J. Ryan Thigpen, Summer J. Brown Formal analysis: Autumn L. Helfrich, J. Ryan Thigpen, Victoria M. Buford-Parks, Summer J. Brown Funding acquisition: J. Ryan Thigpen

Funding acquisition: J. Ryan Thigpen **Investigation:** Autumn L. Helfrich, Ryan C. Goldsby

Methodology: J. Ryan Thigpen, Victoria M. Buford-Parks, Nadine McQuarrie, Ryan C. Goldsby

Resources: J. Ryan Thigpen Software: Victoria M. Buford-Parks, Nadine McQuarrie

Supervision: J. Ryan Thigpen Validation: Autumn L. Helfrich, J. Ryan Thigpen, Nadine McQuarrie Visualization: Autumn L. Helfrich

© 2024. American Geophysical Union. All Rights Reserved.

Constraining Displacement Magnitude on Crustal-Scale Extensional Faults Using Thermochronology Combined With Flexural-Kinematic and Thermal-Kinematic Modeling: An Example From the Teton Fault, Wyoming, USA

Autumn L. Helfrich¹, J. Ryan Thigpen¹, Victoria M. Buford-Parks², Nadine McQuarrie², Summer J. Brown¹, and Ryan C. Goldsby¹

¹Department of Earth and Environmental Sciences, University of Kentucky, Lexington, KY, USA, ²Department of Geology and Environmental Science, University of Pittsburgh, PA, USA

Abstract Constraining the geometry and displacement of crustal-scale normal faults has historically been challenging, owing to difficulties with geophysical imaging and inability to identify precise cut-offs at depth. Using a modified workflow previously applied to contractional systems, flexural-kinematic (Move) and thermal-kinematic (Pecube) models are integrated with apatite (U-Th)/He (AHe) and apatite fission track (AFT) data from Teton footwall transects to constrain total Teton fault displacement (D_{max}). Models with slip onset at ~10 Ma and flexure parameters that best match the observed Teton flexural profile require $D_{max} > 8$ km to produce young (<10 Ma) AHe ages observed at low elevation footwall positions in the Tetons. For the same slip onset, models with D_{max} of 11–13 km provide the best match to observed AHe data, but displacements ≥ 16 km are required to produce observed AFT ages (13.6–12.0 Ma) at low elevations. A more complex model with slow slip onset at ~25 Ma followed by faster slip at ~10 Ma yields a good match between modeled and observed AHe ages at a D_{max} of 13–15 km. However, this model predicts low elevation AFT ages 6–8 Ma older than observed ages, even at D_{max} values of 16–17 km. Based on this analysis and integration with previous studies, we propose a unified evolution wherein the Teton fault likely experienced 11–13 km of Miocene-recent displacement, with AFT data likely indicating a pre-to early Miocene cooling history. Importantly, this study highlights the utility of using integrated flexural- and thermal-kinematic models to resolve displacement histories in extensional systems.

1. Introduction

The Basin and Range province in the western United States is characterized by crustal-scale extensional faulting, with the "basins" and "ranges" developing as the down-dropped hanging walls and the uplifted footwalls, respectively, in these normal fault systems (Wernicke, 1981). Despite decades of research focused on the initiation and growth evolution of crustal-scale normal faults in this system (Colgan et al., 2006, 2008; Curry et al., 2016; Densmore et al., 2004), estimates of the finite extensional strain accommodated by these structures has been mostly limited to cross-section reconstructions constrained by near-surface structural geometries (Colgan et al., 2008; Long, 2019; Rodgers et al., 2002) or studies that integrate limited available geophysical imaging (Allmendinger et al., 1983, 1987a, 1987b; Brown et al., 1987; Long, 2019; Velasco et al., 2010). These challenges aren't simply limited to Basin and Range normal faults, as interpreting the kinematic and tectonic evolution of crustal-scale normal faults across a range of settings has remained persistently challenging (Galadini & Galli, 2000; Ortner et al., 2022). Like normal faults and low-angle detachments of the Basin and Range, many of these structures yield limited cut-offs and other markers to determine offset, and thus identifying techniques that allow the structural evolution of these systems to be characterized could provide significant uplift for extensional studies. Numerous studies applying a range of techniques (e.g., geophysics, stratigraphy, thermochronology, etc.) have estimated the magnitude and timing of footwall uplift for Basin and Range normal faults (Brown et al., 2017; Ehlers et al., 2003; Stockli et al., 2002, 2003; Thigpen et al., 2021) but linking footwall uplift to total displacement magnitude requires a kinematic model that can be used to evaluate the isostatic flexural response of crustal-scale normal fault evolution.

As an example, the active Teton fault in northwestern Wyoming accommodates crustal-scale intraplate extension in the northeasternmost Basin and Range province (Figure 1). The Teton fault lies at the junction of four distinct

HELFRICH ET AL. 1 of 29



Writing – original draft: Autumn L. Helfrich Writing – review & editing: J. Ryan Thigpen, Nadine McQuarrie tectonic provinces (Figure 1a; Basin and Range, Snake River plain/Yellowstone hotspot track, Laramide Gros Ventre uplift, Sevier fold-thrust belt), yet despite being one of the most prominent crustal-scale normal faults in the U.S., both the age of fault slip onset and total (and episodic) displacement along the Teton fault has remained controversial (Anders & Sleep, 1992; Anders et al., 1989; Barnosky, 1984; Behrendt et al., 1968; Brown et al., 2017; Byrd et al., 1994; Lageson, 1992; Pierce & Morgan, 1990, 1992, 2009; Thigpen et al., 2021). Given this dynamic setting, the Teton-Yellowstone region has been subjected to varying levels of Mesozoic to early Tertiary crustal shortening, late Tertiary to Quaternary extension, normal faulting, and volcanism, crustal uplift and subsidence associated with the Yellowstone volcanic province (Smith et al., 1990, 1993). The Teton Range also lies within the Intermountain Seismic belt (Smith & Sbar, 1974), where Miocene-Quaternary normal faults generate earthquakes in response to intraplate extension (White et al., 2009). Evidence for Quaternary motion on the Teton fault is observed in post-glacial moraine ruptures, with total offsets of 3–52 m (Byrd et al., 1994; Smith et al., 1993; Thackray & Staley, 2017). Recent fault motion is documented by terrestrial and lacustrine paleoseismology studies along the modern Teton fault scarp (Byrd & Smith, 1990; DuRoss et al., 2019, 2021; Larsen et al., 2019; Smith et al., 1993; Zellman et al., 2018, 2019a, 2019b).

In this study, we use the Teton fault as a test case of an integrated workflow to constrain total displacement using thermochronology and flexural-kinematic (Move, Petroleum Experts) and thermal-kinematic (Pecube, Braun, 2003) modeling. The *Pecube* methodology utilized here follows that of McQuarrie and Ehlers (2015). In this study, the models are used to derive fault evolution scenarios that most closely reproduce: (a) the flexural wavelength and amplitude of the footwall uplift and the resulting erosional history, (b) the flexural wavelength of the adjacent hanging wall basin, and (c) the resultant exhumation and cooling history that can be compared with thermochronologic dates from Mount Moran, which is considered to represent the locus of maximum displacement for the Teton fault (e.g., Brown et al., 2017; Thigpen et al., 2021). To do this, flexural-kinematic models are used to evaluate the subsurface fault geometry and the effective elastic thickness of the crust based on comparisons between the modeled and observed isostatic response, which controls the width of the flexural uplift and that of the adjacent hanging wall basin. By using the subsurface geometry of the fault (and the flexural parameters) that yield a the best match to surface observables such as the flexural-wavelength of the footwall uplift, fault displacement magnitude and fault slip timing can be further evaluated using comparisons between AHe and apatite fission track (AFT) cooling data and AHe/AFT age predictions derived from thermalkinematic models. The results of this study provide new insight for the controversial kinematic evolution of the Teton fault and the resulting footwall topographic history. Constraining the total displacement on the Teton fault and the age of slip onset is critical for understanding the fault activity and slip history, the lateral extent of this structure (e.g., Brown et al., 2017), and the consequences this may have for seismic hazard evaluation in the Teton-Yellowstone region (e.g., White et al., 2009). More broadly, these models help define the range of critical parameters that directly influence the magnitude of footwall exhumation, the correlation between footwall uplift and hanging wall drop, and the resultant cooling histories in extensional settings like the Basin and Range.

2. Geologic Setting

The Teton region preserves a tectonostratigraphy composed of Late Archean para- and orthogneiss and Proterozoic monzonitic, mafic, and ultramafic basement rocks unconformably overlain by Cambrian-Miocene sedimentary units and capped by Eocene volcanoclastic flows of the Absaroka Volcanic Supergroup and Pliocene to recent volcanic flow and tuff units associated with the adjacent Yellowstone caldera system (Christiansen et al., 1978; Love & Albee, 1972; Love & Reed, 2000; Love et al., 1978, 1992). The Teton fault, interpreted to be active from Miocene to recent, forms the eastern margin of the modern Teton Range (Brown et al., 2017; Byrd et al., 1994; Edmund, 1951; Horberg et al., 1949; Love & Reed, 1971). The uplifted footwall west of the Teton fault is primarily composed of Archean-Proterozoic basement and Cambrian-Permian sedimentary units separated by the "Great Unconformity," which is exposed primarily in the northern and southern end of the Teton Range. At Mount Moran, which is composed almost entirely of basement lithologies, the unconformity is famously exposed immediately below the summit, where the mountain is capped by a thin veneer of Cambrian Flathead Quartzite (Love et al., 1992).

Extensive geologic mapping in the footwall of the Teton fault yields precise thicknesses estimates for Paleozoic-Jurassic sedimentary units (Love & Albee, 1972; Love & Love, 2000; Love & Reed, 1975, 2000; Love et al., 1992; Reed, 1973). This, coupled with exposure of the basal Cambrian unconformity on the summit of

HELFRICH ET AL. 2 of 29

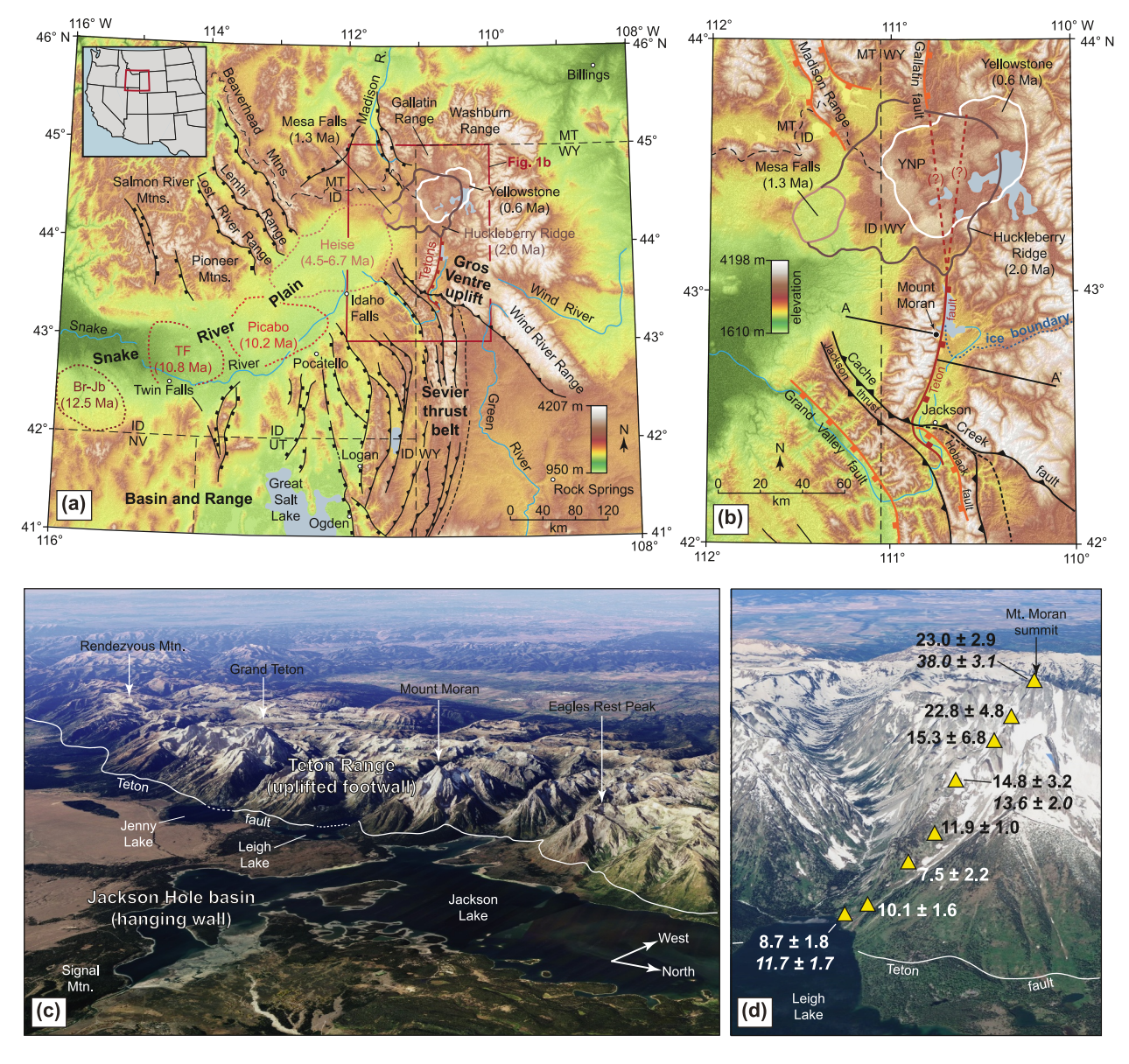


Figure 1. (a) Regional digital elevation model (DEM) of the Teton-Yellowstone region, which represents the confluence of the northeastern Basin and Range, the Yellowstone hotspot track, the Sevier thrust belt, and the Wind River Range basement uplift. The position and timing of plume eruptions along the Snake River plain derived from Pierce and Morgan (1992, 2009). (b) DEM of the study area, showing the position of Basin and Range normal faults (orange), the Teton fault (red), Sevier and Laramide thrust faults (black), the three most recent caldera eruptions (Yellowstone-Lava Creek, white; Mesa Falls, light brown; Huckleberry Ridge, dark brown). Thigpen et al. (2021) projections of the paleo-Teton fault across the modern Yellowstone caldera are also shown. Line A–A' shows the position of the swath topographic profile in Figure 5. (c) Google Earth image of the Teton Range from the northeast, showing the locations of Mount Moran, Grand Teton, Rendezvous Mountain, Eagles Rest Peak, Jenny Lake, Leigh Lake, Jackson Lake, and Signal Mountain. The approximate position of the Teton fault, the uplifted footwall represented by the Teton Range, and the downdropped hanging wall represented by the Jackson Hole basin are also shown. (d) Zoomed in Google Earth image of Mount Moran, showing the location of samples along the Mount Moran transect of Brown et al. (2017) and Thigpen et al. (2021). The average AHe ages (±1s) and apatite fission track central ages (±2s, *italicized*) are included for each sample. Details for all samples are included in the supplementary material (Tables S1 and S2 in Supporting Information S1).

Mount Moran, provides relatively robust constraints for the total thickness of stratigraphy eroded from above the uplifted basement units in the footwall near Mount Moran. In the hanging wall, however, stratigraphic cut-offs are much more limited, as development of the active graben system has led to burial of most footwall units beneath glacial deposits of the Bull Lake (~150 ka) and Pinedale (~14 ka) advances (Pierce et al., 2018). Exceptions to this include multiple buttes that rise out of the Jackson Hole basin. Signal Mountain, which lies ~7 km east of Mount Moran (Figure 1c), exposes a westward dipping interlayered sequence of Eocene and Pliocene volcanic/

HELFRICH ET AL. 3 of 29





Table 1Previous Estimates of Teton Fault Displacement

Study	Displacement (km)	Criteria
Blackwelder (1915)	>3.0	Physiographic, stratigraphic
Edmund (1951)	2.1–4.3	Stratigraphic, structural
Fryxell et al. (1941)	2.4	Stratigraphic, geomorphic
Lavin and Bonini (1957)	5.0-6.0	Gravity
Behrendt et al. (1968)	7.0	Gravity, seismic refraction
Tibbetts et al. (1969)	7.0	Seismic refraction
Love and Reed (1971)	7.6–9.1	Stratigraphic
Love (1977, 1987)	9.0-11.0	Stratigraphic
Gilbert et al. (1983)	2.1-2.9	Huckleberry (Kilgore) tuff
Roberts and Burbank (1993)	3.5	Thermochronology
Byrd et al. (1994)	2.5–3.5	Gravity, seismic refraction, geodetic data
Brown et al. (2017)	>6.0	Thermochronology
Thigpen et al. (2021)	>11.4-12.6	Thermochronology, flexural modeling

10.1029/2024TC008308

Note. Modified from Byrd et al. (1994).

clastic (Hominy Peak Formation, 48.6 ± 0.7 Ma; Kilgore Tuff, 5.57 ± 0.19 Ma) and Miocene sedimentary units, including the Teewinot and Colter Formations (Love, 2004; Love et al., 1992). The dip of these hanging wall units is interpreted to reflect post-depositional rollover due to motion on the underlying Teton fault. Although some studies have used westward projection of these units to estimate more recent Teton displacement (e.g., Gilbert et al., 1983; Smith et al., 1993), the lack of geophysical imaging beneath the glacial units between Signal Mountain and Mount Moran represents a serious limitation for this approach.

These challenges with subsurface imaging have led to a large range of Teton fault displacement estimates (2.1–12.6 km) and slip onset ages of (2–28 Ma; Table 1). The lowest estimates for Teton fault maximum displacement (D_{max}) are derived from integrated stratigraphic and geophysical constraints for post-depositional rotation of either the ~2 Ma Huckleberry Ridge tuff (2.5–3.5 km, Byrd et al., 1994) or the ~4.45 Kilgore-Heise tuff (3.8–6.7 km displacement; Gilbert et al., 1983; Smith et al., 1993) in the Teton fault hanging wall. Other stratigraphic studies that rely on extrapolated cut-offs of the Precambrian-Paleozoic unconformity in Jackson Hole basin yield Teton D_{max} values of 6–9 km (Love & Reed, 1971). Earlier gravity (Lavin & Bonini, 1957) or integrated gravity and seismic refraction studies (Behrendt et al., 1968; Tibbetts et al., 1969) yield D_{max} values of 5–7 km based on an interpreted depth to basement of ~5 km immediately to the east of the Teton fault, however regional subsurface mapping (e.g., Blackstone, 1993; Wyoming State Geological Survey, 2022) indicates that the depth to basement in that area is likely >6.5 km.

Low temperature thermochronology has also been used in earlier attempts to constrain the cooling and uplift history of the Teton Range and displacement on the Teton fault (e.g., Brown et al., 2017; Roberts & Burbank, 1993; Thigpen et al., 2021). Low temperature thermochronometers such as apatite (U-Th)/He (AHe) and AFT record the time that rock particles passed through closure temperatures (T_c) zones of 80–40°C and 120–60°C, respectively, and therefore they can provide critical information about the thermal history of rock particles in active tectonic settings (Ehlers & Farley, 2003; Green et al., 1989; Ketcham et al., 1999, 2007; Laslett et al., 1994; Rahn & Grasemann, 1999; Stüwe et al., 1994). Brown et al. (2017) used inverse thermal history modeling (QTQT; Gallagher, 2012) of AHe data collected along an elevation transect at Mount Moran to establish a fault onset timing of 13–8 Ma. Because AHe ages at the bottom of the transect were generally younger than the onset age and thus were considered reset, that study inferred a minimum of 2 km of uplift, representing the present-day total relief, must have occurred. Numerical models of some simple normal fault systems (e.g., Thompson & Parsons, 2009) indicate that footwall uplift accounts for 33% of the total displacement, with the rest accommodated by hanging wall drop. Brown et al. (2017) combined their footwall uplift estimates with this value to estimate a total minimum Teton fault offset of ~6 km. Thigpen et al. (2021) integrated new AHe data with the pre-existing data of Brown et al. (2017) into new inverse thermal history models that included revised geothermal

HELFRICH ET AL. 4 of 29



gradient estimates based on surface heat flow values (Blackwell & Richards, 2004). This was recognized to be critical for thermal history modeling, as surface heat flows increase considerably from south to north along strike in the Teton Range. The results of these new inverse and geothermal gradient models were then combined with a simple flexural-kinematic model of Helfrich (2020) to produce Teton fault displacement estimates of 11.4–12.6 km. Adding to the controversy, both Brown et al. (2017) and Thigpen et al. (2021) used their displacement estimates and empirical fault length-displacement scaling relationships to propose that the Teton fault was originally much longer and likely extended across the modern Yellowstone hotspot track prior to ~2 Ma. However, because these estimates rely on a suite of assumptions that may not encapsulate the geodynamic evolution of the Teton region specifically, uncertainty remains in these displacement estimates.

3. Methods

Research on Basin and Range normal faults surrounding the Snake River plain has led to a growing understanding of the overall geometry and behavior of normal faults and the relationship between fault length, total displacement, and footwall uplift in extensional terranes (Anders & Sleep, 1992; Anders et al., 1989; Byrd et al., 1994; Densmore et al., 2004; McQuarrie & Rodgers, 1998; Pierce & Morgan, 1992, 2009). In extensional terranes like the Basin and Range, thinning of the upper crust along crustal-scale normal faults produces an isostatic response that results in flexural uplift of the normal fault footwall coeval with hanging wall drop due to extension (Beaumont, 1979; Turcotte, 1979; Walcott, 1970; Watts et al., 1982). The magnitude of footwall uplift and the corresponding crustal length scale over which this occurs are directly impacted by lithospheric flexural rigidity, total fault displacement, fault dip, and the depth to detachment and/or depth at which the fault becomes listric (e.g., Densmore et al., 2004). Because of this, it is possible to assess the isostatic behavior of the upper crust by testing a range of flexural rigidities, fault geometries, and total slip magnitudes.

To evaluate the range of displacement scenarios, 2-D flexural-kinematic and thermal-kinematic models are used to forward model the isostatic, erosional, and thermal evolution of the Teton fault and Teton Range. In the first phase of modeling, we complete flexural-kinematic models that consider sequential displacement of 2–17 km to exceed the entire spectrum of proposed Teton fault D_{max} values proposed by previous studies. A range of parameters, including near-surface fault dip, depth to listric detachment (Z_d), and effective elastic thickness (T_e), and T_{max} were evaluated in the flexural-kinematic models (Figure 2a). In the second phase of modeling, we choose the flexural-kinematic model that best approximates the observed flexural characteristics of the Teton Range near Mount Moran for thermal-kinematic modeling scenarios. The thermal-kinematic models yield predicted thermochronologic dates for each displacement scenario that can be compared with thermochronology data from the Teton Range. Specifically, modeled derived dates are compared to AHe and AFT ages from the footwall transect of Brown et al. (2017) and Thigpen et al. (2021) near Mount Moran (Figure 1d and Tables S1 and S2 in Supporting Information S1), which is interpreted by those studies to record T_{max} for the Teton fault.

3.1. Flexural-Kinematic Modeling

Flexural-kinematic models were produced using Petroleum Experts Move software. Fault displacement in *Move* is forward modeled using the fault parallel flow algorithm (Egan et al., 1997; Kane et al., 1997), which involves translation of hanging wall particles along flow lines parallel to the fault plane while maintaining line lengths in the hanging wall. Fault slip is implemented in either 1 or 2 km increments. Each displacement increment involves multiple steps (Figure 2b), including: (a) displacement along the model Teton fault, (b) flexural-isostatic adjustment of the deformed crust, (c) erosion of the uplifted footwall, (d) flexural-isostatic adjustment of the eroded crustal profile, and (e) sediment deposition in the hanging wall basin. During the entire process, an *x*–*y* point cloud with a grid spacing of 0.5 km is also deformed along with the section to produce particle vector fields that are used as inputs for the thermal-kinematic models.

For the flexural-isostatic adjustments, the difference in the cross-sectional area of material (as a 2-D proxy of volume) between the deformed topographic surface and the topography of the previous step represents the flexural-isostatic load to be accommodated. When the load is removed or "unloaded," the footwall rises isostatically by a quantity dependent on the flexural properties of the lithosphere. The flexural isostatic response to unloading using a continuous 2D beam is described by Watts (2001):

HELFRICH ET AL. 5 of 29



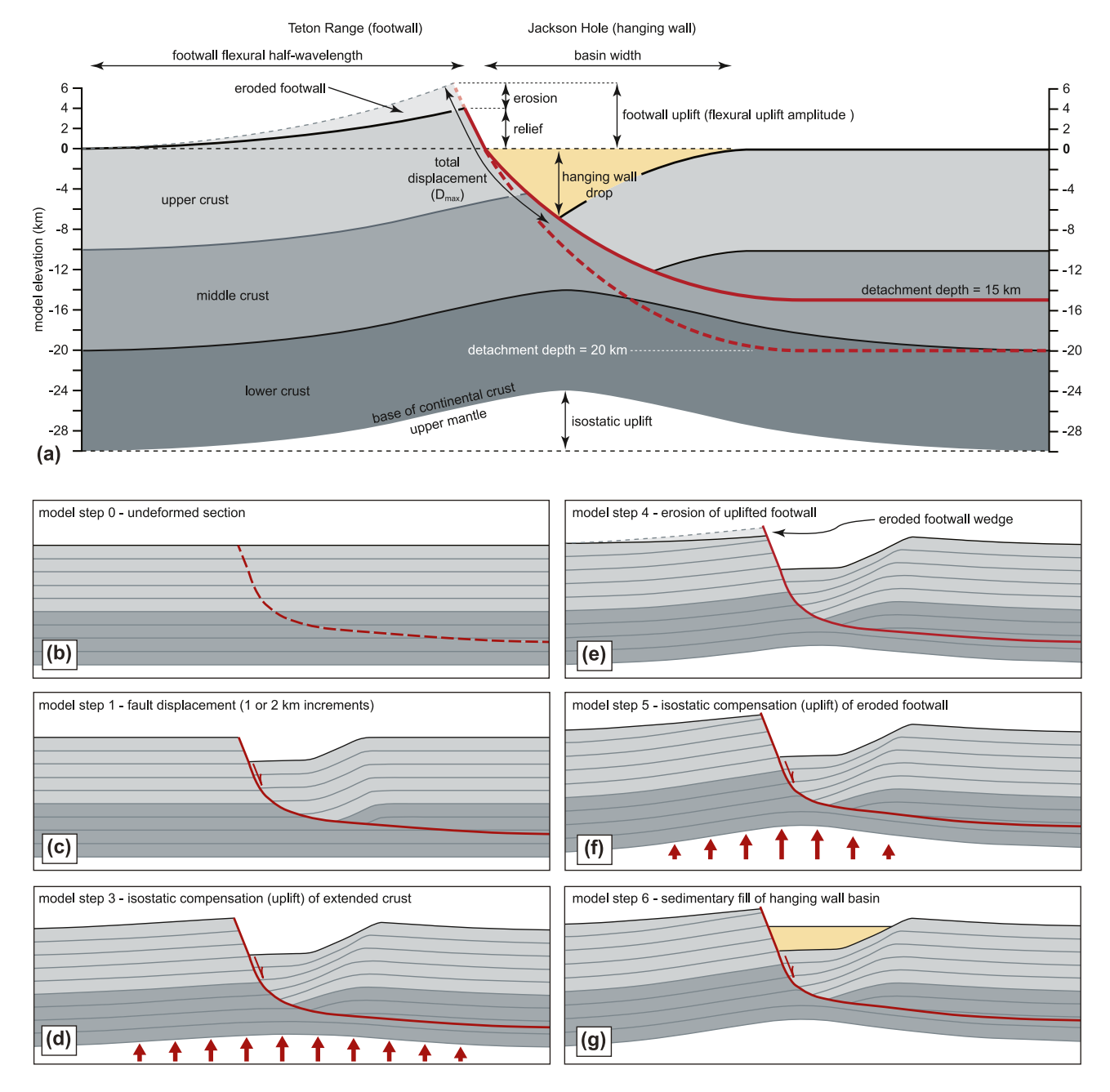


Figure 2. (a) Schematic set-up, parameters, and components of flexural-kinematic models. Normal fault displacement is accommodated both by hanging wall drop and isostatic footwall uplift. Modeled normal fault geometries are characterized by a range of near surface fault dips (45, 60, and 70°), and two listric detachment depths (15 or 20 km). (b)–(g) Sequence of steps involved in the flexural-kinematic forward modeling workflow. (b) Initial model fault geometry controlled by near surface fault dip and listric detachment depth. (c) Fault displacement applied as either 1 or 2 km increments in each step. Hanging wall particle motions are prescribed using the fault parallel flow mechanism in *Move*. (d) After each increment of displacement, isostatic uplift of extended crust is calculated according to the process described in Methods. (e) Following the post-displacement isostatic adjustment, the model footwall is incrementally eroded, with the magnitude of erosion at each time step determined by the number of time steps and the total erosion thickness prescribed for each model. (f) Isostatic response to erosional unloading is calculated using the same methodology in panel (d). (f) In the final step for each displacement increment, the hanging wall accommodation space remaining after fault motion and isostatic adjustment is filled to the elevation of the model zero datum. The basin sedimentary fill has a constant material density of 2,700 kg m⁻³ and depth-dependent compaction is not considered here. All steps are then repeated for each increment of displacement.

HELFRICH ET AL. 6 of 29



$$q = D \frac{d^4 w}{dx^4} + (\rho_m - \rho_c) g w$$

where q is the applied vertical load (N m⁻²), D is the flexural rigidity, ρ_m is the density of the mantle (3,300 kg m⁻³), ρ_c is the density of the eroded crustal material (2,700 kg m⁻³), w is the vertical deflection of the beam, and g is the acceleration due to gravity (9.81 m s⁻²). Lithospheric flexural rigidity D is described by:

$$D = \frac{ET_e^3}{12(1-\nu^2)}$$

where E is Youngs modulus (70 MPa for all models), T_e is the effective elastic thickness (Lowry & Smith, 1994; Tesauro et al., 2015; Watts & Burov, 2003), and ν is Poisson's ratio. The effective elastic thickness of a thin plate overlying a fluid is characterized by Turcotte and Schubert (2002):

$$T_e = M_e \, 12 \, (1 - \nu^2) \, EK^{1/3}$$

where elastic thickness is described by the bending moment (M_e), Poisson's ratio, and curvature (K). In the Teton footwall, effective elastic thickness (T_e) values of 5–15 km have been estimated based on analysis of gravity and topography (Lowry & Smith, 1994) and regional heat flow, lithosphere composition (and age), regional stress orientations, and earthquake focal depth (Lowry & Smith, 1995). Accordingly, the flexural-kinematic models presented here evaluate T_e values of 5, 10, and 15 km. Also, because limited geophysical imaging of Basin and Range normal faults (e.g., Chávez-Pérez et al., 1998; Velasco et al., 2010; Von Tish et al., 1985; Wernicke & Burchfiel, 1982) has indicated that they are commonly steeply dipping (45–70°) near the surface and flatten into shallow dipping listric detachments at depth, the impact of varying these parameters was also tested in our flexural-kinematic models. In this workflow, near surface dip was varied between 45° and 70° and depth to listric detachment (Z_d) was varied between 15 and 20 km (e.g., Mohapatra & Johnson, 1998; Smith & Bruhn, 1984). All flexural-kinematic parameters and model variants are shown in Table 2.

In the model workflow, erosion of the footwall uplift is implemented with each displacement increment, with the maximum thickness of material eroded from the highest elevation part of the model profile. The eroded thickness then decays to zero down the flexural slope (to the left) of the model topography (Figure 2a). The maximum thickness eroded for each increment represents a percentage of the total model erosion distributed equally throughout the model evolution. The unconformable contact between Late Archean basement gneiss and basal Cambrian Flathead Sandstone on the summit of Mount Moran indicates that >2.0 km of Paleozoic-Cretaceous section has been eroded from above Mount Moran based on stratigraphic thicknesses derived from detailed mapping. Specifically, this includes stratigraphic thicknesses of ~1.4 km for Cretaceous units (Thermomopolis Shale, Frontier Formation, Cody Shale, and Bacon Ridge Sandstone), ~120 m of Jurassic units (Sundance Formation), ~300 m for Triassic units (Dinwoody and Chugwater Formation), and 1.0–1.3 km for Paleozoic units (Christiansen et al., 1978; Love et al., 1992). Because of this, most flexural-kinematic models include total eroded thicknesses of ~2.0–2.3 km over the entire model run. The only exception to this is flexural-kinematic Model 3, where the flexural response produced a total footwall uplift magnitude of only 1.7 km, which would have resulted in complete removal of the footwall if the 2.0–2.3 km of erosion thickness was applied.

Model topographic profiles are compared with a swath topographic profile from the modern Teton Range (Line A–A'; Figure 1b). The swath profile was constructed using a 10 m digital elevation model and the SwathProfiler ArcGIS add-in (Pérez-Peña et al., 2017). The SwathProfiler calculates maximum, minimum, and mean elevation profiles for 50 equally spaced topographic profiles within a 6,000 m wide swath normal to the Teton fault in the vicinity of Mount Moran. The resultant mean swath profile of the observed topography is then compared with the range of results from the flexural-kinematic models to define a reference case model that displays the best-fit between the modeled and observed topography. The model that best matches the observed flexural profile of the Teton Range is then carried forward for thermal-kinematic modeling.

HELFRICH ET AL. 7 of 29



Tectonics 10.1029/2024TC008308

Table 2								
Flexural-	Kinematic	Numerical	Parameters	and Dimensions,	Model	Variants,	and Summary of Results	
C1 1 1	1.1							

Global model parameters		
Model domain	x = 310 km	y = 30 km
Node spacing	0.5 km	
Crustal density (ρ_c)	$2,700 \text{ kg m}^{-3}$	
Mantle density (ρ_m)	$3,300 \text{ kg m}^{-3}$	

Model variants	Near- surface fault dip (degrees)	Effective elastic thickness (T_e, km)	Listric detachment depth (km)	D_{max} (km)	FW flexural width (km)	HW basin width (km)	Total footwall uplift (km)	Eroded thickness (km)	FW relief (km)
Model 1	70	5	20	13	41.0	22.1	4.5	2.0	2.5
Model 3	60	15	20	13	93.3	23.9	1.7	1.4	0.3
Model 4	45	15	20	13	93.0	26.5	2.5	2.3	0.2
Model 5	45	10	20	13	98.1	26.9	2.9	2.0	0.9
Model 6	70	10	15	13	73.8	16.5	2.8	1.9	0.9
Model 7	70	15	20	13	95.5	22.4	2.7	1.9	0.8
Model 10	60	5	20	13	50.6	21.6	4.0	2.1	1.9
Model 11	45	5	15	17	65.1	17.7	4.7	2.2	2.5
Model 12	60	5	15	17	60.0	18.5	4.8	2.1	2.7
Model 13	70	5	15	17	58.4	10.3	5.1	2.1	3.1

Note. D_{max}—maximum model displacement. FW—footwall. HW—hanging wall.

3.2. Thermal-Kinematic Modeling

In the final step of the modeling workflow, a reference case flexural-kinematic model is coupled with a thermal-kinematic *Pecube* model (Braun, 2002, 2003; Braun et al., 2012). Here, we use the modified *Pecube-D* code (McQuarrie & Ehlers, 2015) that incorporates velocity fields from the flexural-kinematic models developed in Move to generate predicted synkinematic footwall cooling histories that can be compared with thermochronology data. To do this, the *Pecube-D* code solves the 2-D heat transport equation for a prescribed kinematic velocity and surface evolution scenario to yield a forward model of the crustal thermal field. In *Pecube-D*, the topographic surface from *Move* is provided at each timestep so that the thermal model is calculated using the evolving flexural-kinematic surface topography. *Pecube-D* scenarios were run using the simulation cluster in the Earth System Dynamics Research Group at the Universitat Tübingen.

All material properties and parameters for thermal-kinematic models are shown in Table 3. The value for the bulk thermal conductivity (3 Wm $^{-1}$ K $^{-1}$) was assigned based on measured data in the Teton Range (Heasler, 1987). Specific heat capacity (880 J kg $^{-1}$ K $^{-1}$) corresponds to a measured mean value for granite (Touloukian et al., 1989). In the *Pecube-D* code, the geothermal gradient is defined by setting an atmospheric lapse rate of 6° C km $^{-1}$ above the model surface (Dirks, 1982; Masbruch et al., 2012) and fixed boundary temperatures for the surface (4° C) and the base of the model at 110 km depth (1,300°C).

Radiogenic heat production in the crust is then prescribed as a surface heat production value (A_o) and optional e-folding depth (e_f) , which describes the exponential decrease in heat production with depth in the model space (McQuarrie & Ehlers, 2015, 2017). For this model, we use an A_o value of 3.5 μ Wm⁻³, which is within the range of global average values for granite, and an e-folding (e_f) depth of 15 km. Combined, these values yield an initial geothermal gradient of 27–25°C km⁻¹ in the upper ~3 km of the model crust. Because subsurface heat flow evolves with time as material motion drives heat advection, we compare final model geothermal gradients with gradients predicted from observed surface heat flow values in the central and northern Teton Range (Blackwell & Richards, 2004; Heasler, 1987). Mantle (3,300 kg m⁻³) and crustal (2,700 kg m⁻³) density values used in flexural-kinematic modeling were also used for thermal-kinematic modeling.

HELFRICH ET AL. 8 of 29



Basal temperature

Table 3	
Parameters Used in	Thermal-Kinematic (Pecube) Models

Parameters Used in Thermal-Kinematic (Pecube) Models						
Property	Model input					
Material properties						
Surface heat production (A_o)	$3.5~\mu\mathrm{W~m}^{-3}$					
Thermal conductivity (k)	$3.0~W~m^{-1}~K^{-1}$					
Specific heat capacity (c)	$880 \text{ J kg}^{-1} \text{ K}^{-1}$					
e-folding depth (e_f)	15 km					
Crust density (pc)	$2,700 \text{ kg m}^{-3}$					
Mantle density (pm)	$3,300 \text{ kg m}^{-3}$					
Upper crustal geothermal gradient (0-5 km)	27–26°C km ⁻¹					
Parameter	Model input					
Numerical parameters						
Model domain	x = 310 km, y = 110 km					
Onset of fault motion	10 Ma					
Model grid spacing	$500 \text{ m} \times 500 \text{ m}$					
Surface T at sea level	4°C					
Atmospheric lapse rate	$6^{\circ}\text{C km}^{-1}$					

1,300°C

Five of the thermal-kinematic models (R1, R2, R3, R5, and R7) use a constant displacement rate, so greater total displacement results in faster average slip rates. Because the oldest AFT central age in the Moran data set is \sim 38 Ma (Brown et al., 2017), the model thermal field is activated at 48 Ma. This produces AFT ages of \sim 38 Ma for samples in or near the AFT partial annealing zone at the onset of fault slip in the case of a simple uplift and exhumation history. In all but one thermal-kinematic model, displacement starts at 10 Ma, based on inverse thermal history modeling results of Thigpen et al. (2021) that indicate rapid footwall cooling starting at \sim 10 Ma. In a final model, fault slip is initiated at \sim 25 Ma and then accelerated at \sim 10 Ma to evaluate a potential earlier uplift onset in the Moran inverse thermal history model of Thigpen et al. (2021).

4. Results

4.1. Flexural-Kinematic Modeling

Ten 2-D models were constructed to evaluate a range of flexural-kinematic parameters for the Teton fault. The final model stage for Models 1, 3, 4–7, and 10–12 are shown in Figure 3. The full flexural-kinematic evolution of Model 13, chosen as the reference model based on the justification detailed later in this section, is shown in Figure 4. The full flexural-kinematic evolution of models summarized in Figure 3 is included in the supplementary material as Figures S1–S9 in Supporting Information S1. A summary of flexural-kinematic results are presented in Table 2 and detailed

results for each model timestep are included in Table S3 in Supporting Information S1. Model results were evaluated against three observational metrics of the present-day Teton topography (Figures 2a and 5), including: (a) the general shape of the Teton footwall uplift, including the flexural half-wavelength and interpreted finite amplitude, (b) the approximate width of the Teton hanging wall (Jackson Hole) basin as derived from the modeled depth to pre-Cenozoic basement (12–17 km, Foster et al., 2010), and (c) the maximum relief of the footwall block, represented by the modern Teton Range, from the Jackson Hole valley floor to the summits of Mount Moran (~1.8 km) and the Grand Teton (~2.2 km). To be considered viable, flexural-kinematic models must approximate the general flexural shape of the Teton footwall uplift and hanging wall basin, yield sufficient uplift on the eastern side of the range to allow for ~2 km of overburden erosion (e.g., Christiansen et al., 1978; Love et al., 1992), and still preserve the observed relief at minimum (1.8–2.2 km).

In all models, uplift, erosion, relief magnitude and footwall flexural half-length increased systematically with increasing increments of modeled Teton fault displacement. These increments of increasing displacement also drive a progressive decrease in the width of the modeled hanging wall basin, as the rollover anticline develops to the east of the basin (to the right in model space). In general, models with T_e values of 10 km (Models 5 & 6) and 15 km (Models 3, 4, and 7) have footwall uplift profiles that yield poor fits when compared with the observed uplift profile (Figures 5a–5c). Additionally, these higher T_e models produced significantly lower total uplift on the eastern side of the range, which considerably limited preserved relief after accounting for the requirement that >2.0 km of overburden must be removed by erosion. Even at modeled fault displacements of 13 km, models with T_e values of 10 and 15 km produced total uplift magnitudes of 1.9–2.0 km and 1.7–2.7 km, respectively, limiting preserved relief to 0.2–1.2 km.

Models with T_e values of 5 km yield the best general fit to the modern flexural profile (Figures 5d–5g) and yield considerably greater uplift magnitudes than models with T_e values of 10–15 km. In the models with T_e values of 10 and 15 km, the longer wavelength of the stronger flexural beam leads to reduction of the uplift amplitude in these models (Figures 5b and 5c). For the 5 km T_e models, varying the near surface fault dip and depth to listric detachment parameters yields minimal variation in model response. In these models, displacement magnitude acts as the primary control on increasing footwall flexural half-wavelength, decreasing hanging wall basin width, and increasing total footwall uplift. Models 12 and 13, which have near surface fault dips of 60° and 70°, respectively, otherwise have identical model parameters and yield virtually indistinguishable results for given intervals of fault

HELFRICH ET AL. 9 of 29



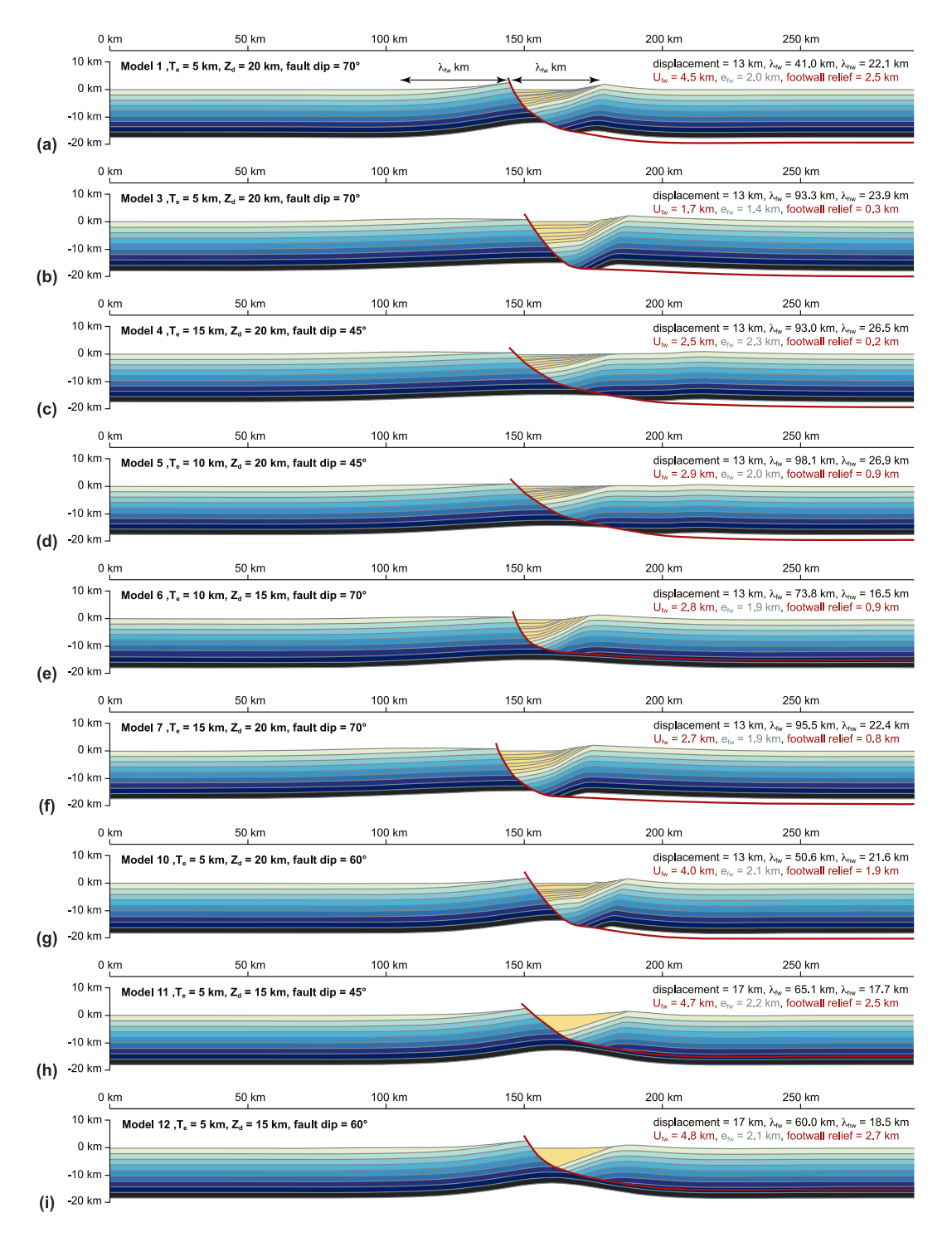


Figure 3. 2-D cross-sections showing the final geometry for flexural-kinematic models. (a) Model 1. (b) Model 3. (c) Model 4. (d) Model 5. (e) Model 6. (f) Model 7. (g) Model 10. (h) Model 11. (i) Model 12. Model parameters are indicated above each cross-section and the results of footwall flexural wavelength, hanging wall basin width, total footwall uplift (U_{fw}) , total erosion (e_{fw}) , and footwall relief are indicated for each model increment. Models include no vertical exaggeration. Full model results showing the geometry at each displacement increment are included in the supplementary material (Figures S1–S9 in Supporting Information S1).

HELFRICH ET AL. 10 of 29



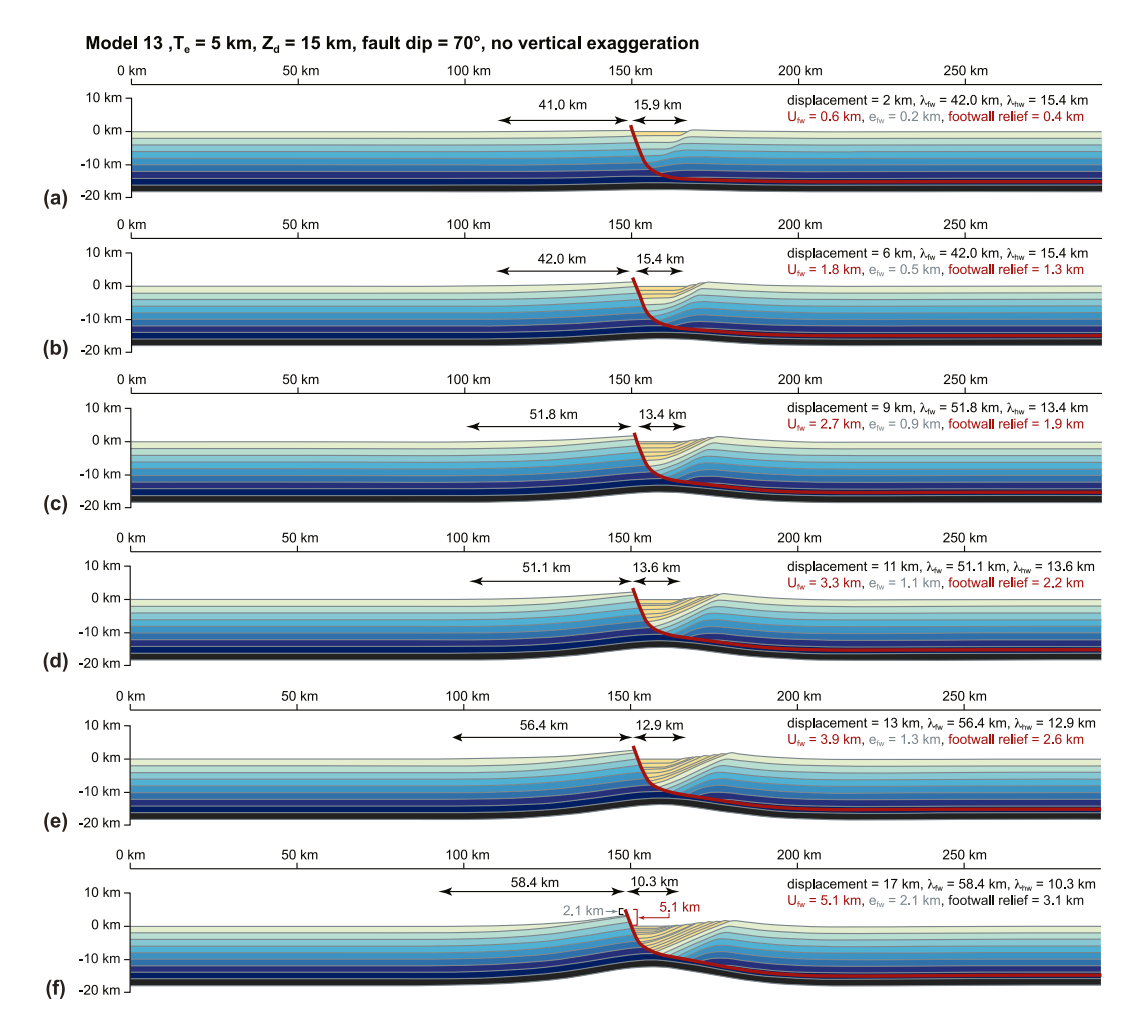


Figure 4. Flexural-kinematic results of Model 13 for selected displacements of (a) 2 km, (b) 6 km, (c) 9 km, (d) 11 km, (e) 13 km, and (f) 17 km. Model parameters are indicated above (a) and the results of footwall flexural wavelength, hanging wall basin width, total footwall uplift ($U_{\rm fw}$), total erosion ($e_{\rm fw}$), and footwall relief are indicated for each model increment. Models include no vertical exaggeration.

displacement (Figures 5f and 5g, Table 2 and Table S3 in Supporting Information S1). Model 11, which has the same parameters as 12 and 13 but with a near surface fault dip of 45° , yields a slightly longer footwall flexural uplift half-wavelength and a considerably wider hanging wall basin than that observed in the Teton swath topography (Figure 5e). Based on these results, Model 13 (Figure 4) was chosen as the reference flexural model for thermal-kinematic modeling, however other models with $T_e = 5$ km, including Models 11 and 12, would likely yield similar results in this workflow.

4.2. Thermal Kinematic Modeling

Six thermal-kinematic models were run; five models were run with constant displacement from 10 Ma to present and $D_{\rm max}$ values of 9 km (R1), 11 km (R2), 13 km (R3), 15 km (R5), and 17 km (R7). A final model (R7_25) was also run to evaluate an earlier displacement initiation at ~25 Ma, followed by accelerated displacement from 10 Ma to present. Slip onset timing for all six models is based on the results of inverse thermal history models from the Teton Range (e.g., Thigpen et al., 2021). As mentioned in the methods, the thermal field in the model is activated at ~48 Ma to replicate the oldest AFT central age from the summit of Mount Moran (e.g., Brown et al., 2017). Thus, when fault slip is initiated at 10 Ma, points that are at $T < T_c$ for a given thermochronometer should yield cooling ages of ~38 Myr, assuming a simple uplift history. Model points that are at $T > T_c$ for a given thermochronometer may be exhumed through T_c during model evolution and thus reflect the time at which this occurs. Because the majority of the model-predicted AHe ages used in this analysis are at $T > T_c$ (i.e., deeper than

HELFRICH ET AL. 11 of 29



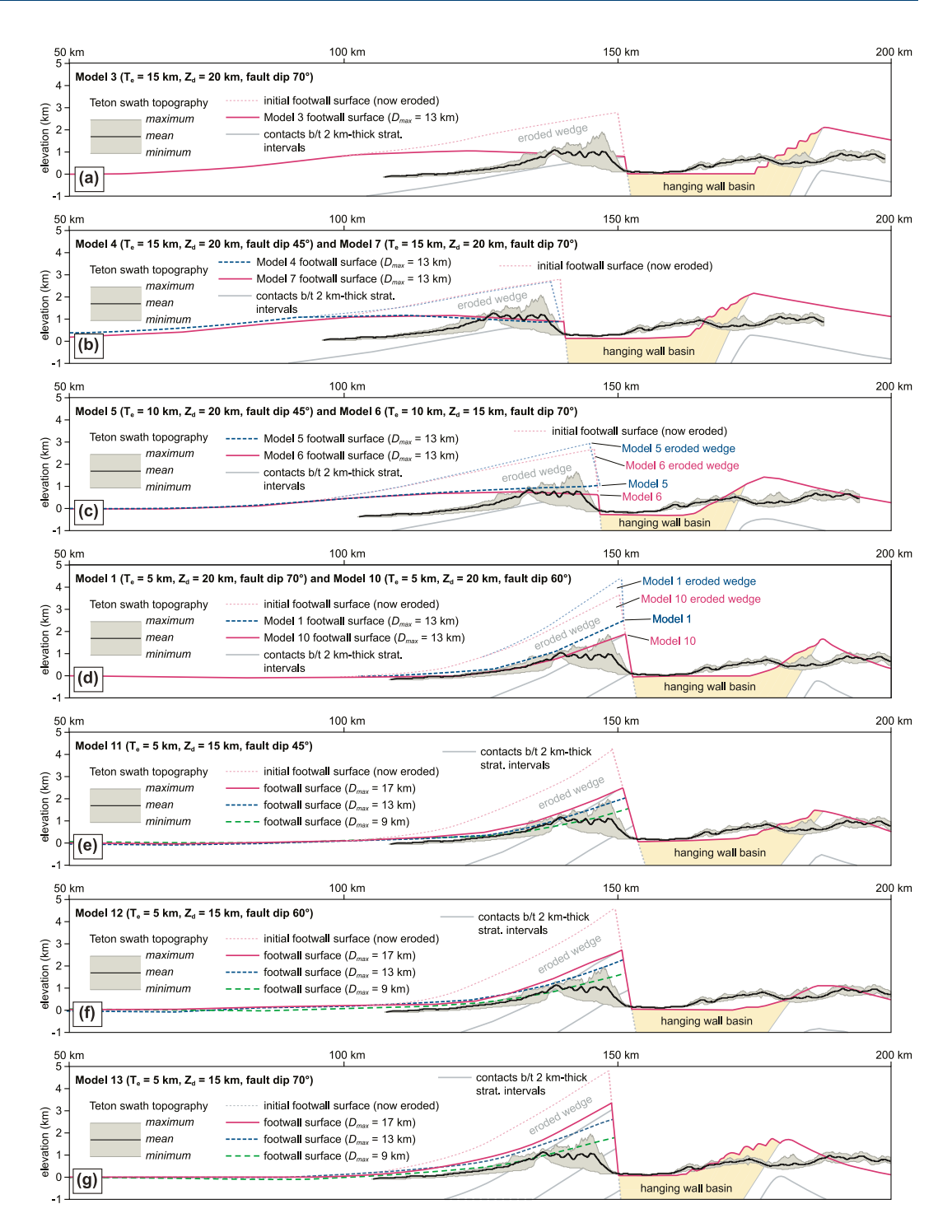


Figure 5. Comparison between flexural-kinematic model results and the swath topographic profile for the Teton Range at Mount Moran. Swath profile shown as heavy black line (mean) and range of elevations shaded in gray. Details for generating the swath topography are discussed in the Methods and flexural-kinematic results are summarized in Table S1 in Supporting Information S1. Model parameters evaluated include effective elastic thickness (T_e), depth to listric detachment (Z_d), and near surface fault dip. Each model result includes the final topography surface at a given increment of D_{max} , the geometry of the eroded material wedge above the modeled Teton Range, and the shape of the flexural half wavelength of the footwall uplift and the hanging wall basin. (a) Model 3. (b) Model 4 and Model 7. (c) Model 5 and Model 6. (d) Model 1 and Model 10. (e) Model 11. (f) Model 12. (g) Model 13.

HELFRICH ET AL. 12 of 29

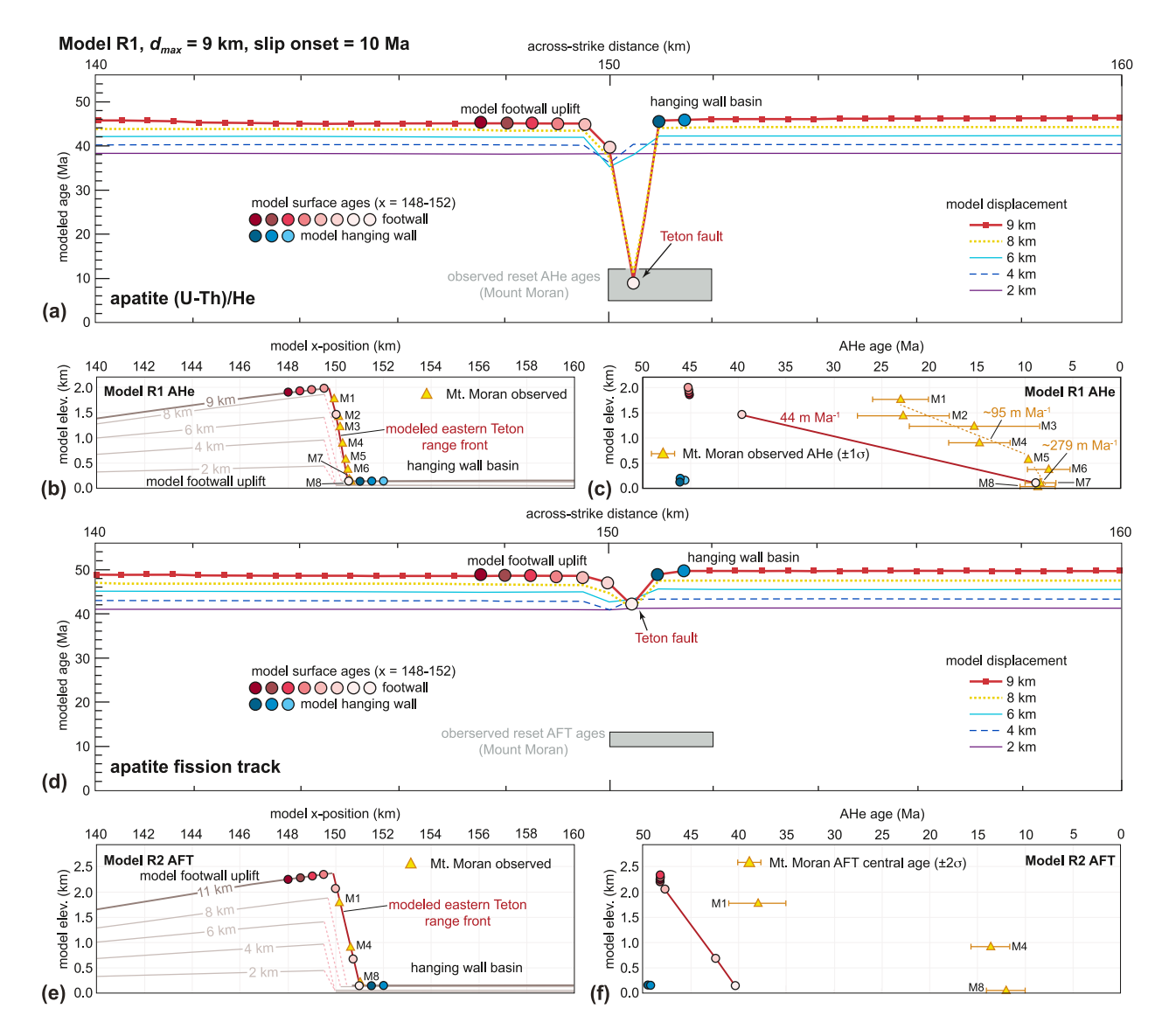


Figure 6. Results of thermal-kinematic Model R1. (a) Predicted apatite (U-Th)/He (AHe) ages (*y*-axis) at the model surface for selected displacement increments from model *x*-positions 140–160 km (*x*-axis) that includes the Teton fault and adjacent footwall uplift and hanging wall basin. Colored circles represent model surface ages for *x*-positions of 148.0–152.0 km, with lighter colors approaching 152.0 km. Blue colors indicate hanging wall surface nodes east of (the right in the model) of the Teton fault. (b) Diagram of model *x*-position and model elevation showing the location the modeled Teton range front at the displacement intervals shown in panel (a) and the relative positions of the model surface ages for the *x* = 148.0–152.0 km positions and the M1–M8 observed thermochronology ages of Brown et al. (2017) and Thigpen et al. (2021). Colored circles correspond to the same colors in panels (a)–(f). (c) Elevation-AHe age plot comparing modeled (colored circles) and observed (yellow triangles with uncertainties) ages. The elevation-age relationship, shown as a linear fit between the two youngest predicted AHe ages that lie on the modeled Teton fault (red line, 44 m Ma⁻¹), represents the unreset slope discussed in the main text. (d) Predicted apatite fission track (AFT) ages at the model surface for the same *x*-positions shown in panel (a). (e) Diagram of model *x*-position and model elevation showing the relative positions of modeled and observed AFT ages. (f) Elevation-AFT age plot comparing modeled and observed AFT ages. Points at the modeled Mount Moran summit and those on the eastern range front representing the Teton fault are linked by a similar red line as (c).

 T_c) at the time of fault initiation and therefore should yield ages younger than fault slip onset, emphasis is here placed on the age-elevation trends of reset samples along the modeled range front rather than the absolute ages determined by the prescribed model start time. Here, we consider fully reset AHe ages to be <10 Ma. A summary of the predicted AHe and AFT cooling ages for the parts of the models that represent the footwall uplift and hanging wall basin (x-positions 140.0–160.0 km) and the modeled range-front transect representing Mount Moran in each scenario are shown in Figures 6–11 and results are summarized in Table 4. Complete results for all thermal-kinematic models, including the sections showing the thermal evolution, are included in the supplementary material (Figures S10–S16 and Table S4 in Supporting Information S1).

HELFRICH ET AL. 13 of 29



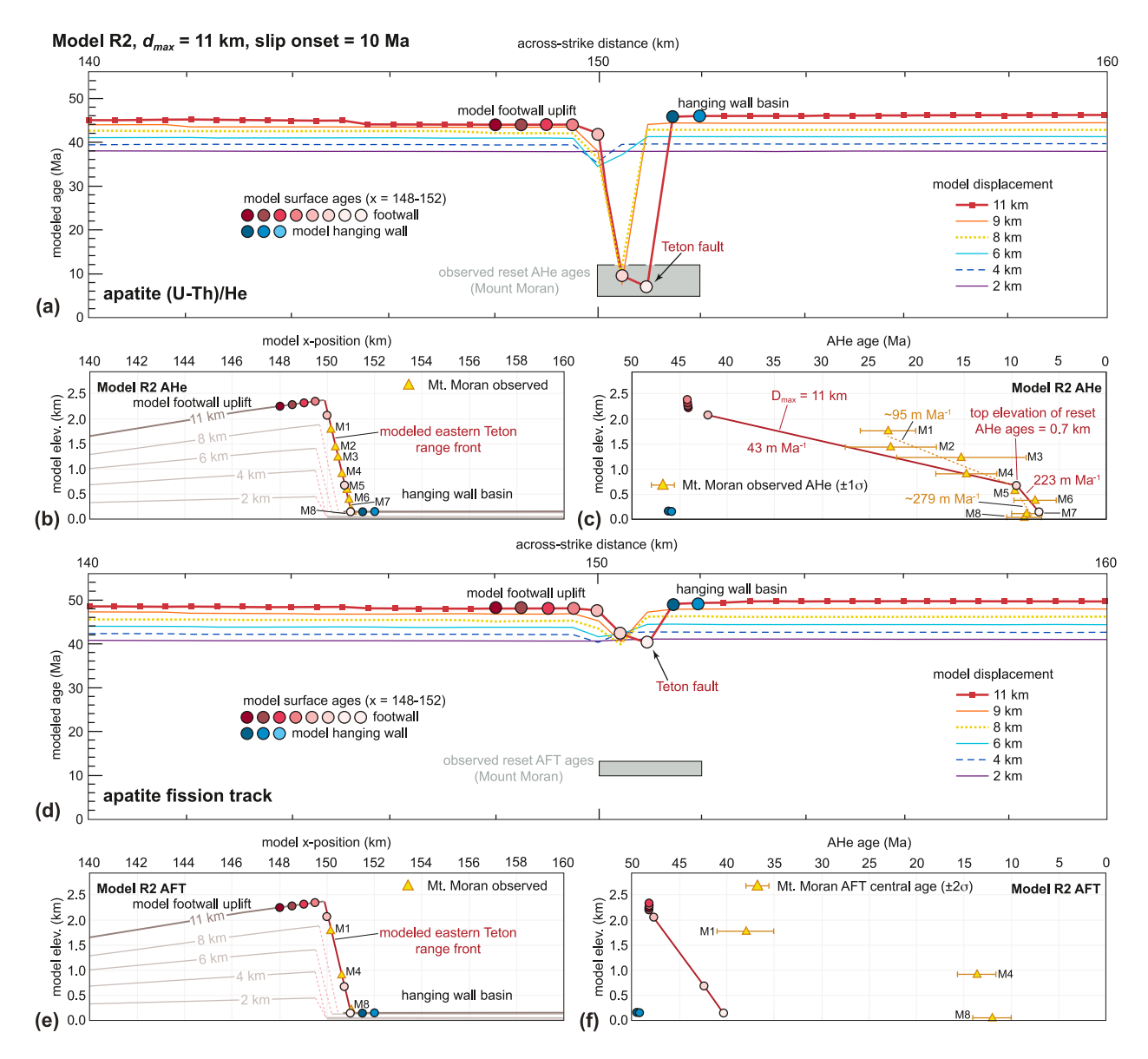


Figure 7. Results of thermal-kinematic Model R2. All parameters and symbols are identical to those in Figure 6. (a) Predicted apatite (U-Th)/He (AHe) ages (*y*-axis) at the model surface for selected displacement increments from model *x*-positions 140–160 km (*x*-axis). (b) Diagram of model *x*-position and model elevation showing the location the modeled Teton range front at the displacement intervals shown in panel (a). Colored circles correspond to the same colors in panels (a)–(f). (c) Elevation-AHe age plot. The two elevation-age relationships slopes (red line) are interpreted to highlight the upper unreset AHe ages (43 m Ma⁻¹) and the 10 Ma-recent fault motion (223 m Ma⁻¹) discussed in the main text. (d) Predicted apatite fission track (AFT) ages at the model surface for the same *x*-positions shown in panel (a). (e) Diagram of model *x*-position and model elevation showing the relative positions of modeled and observed AFT ages. (f) Elevation-AFT age plot comparing modeled and observed AFT ages. Points at the modeled Mount Moran summit and those on the eastern range front representing the Teton fault are linked by a similar red line as (c).

4.2.1. Constant Slip Displacement (Models R1, R2, R3, R5, and R7)

Modeled AHe and AFT cooling ages and age trends produced by thermal-kinematic models are controlled by the prescribed thermal model onset (\sim 48 Ma), the fault slip onset (either 25 or 10 Ma), the magnitude of total displacement, the slip rate as a function of displacement magnitude (e.g., greater displacement magnitudes require higher slip rates), and the prescribed thermal parameters that control geothermal gradient and the degree of advectionary heat transport. In all thermal-kinematic models, the thermal parameters yield an initial steady-state geothermal gradient of \sim 27°C km⁻¹ for the uppermost crust (Figure 12). With the onset of fault slip, footwall uplift and exhumation drive transient modification to the footwall isotherm geometry manifested in two ways. First, uplift of the crustal section leads to footwall heat advection in the middle and upper crust, which is apparent

HELFRICH ET AL. 14 of 29

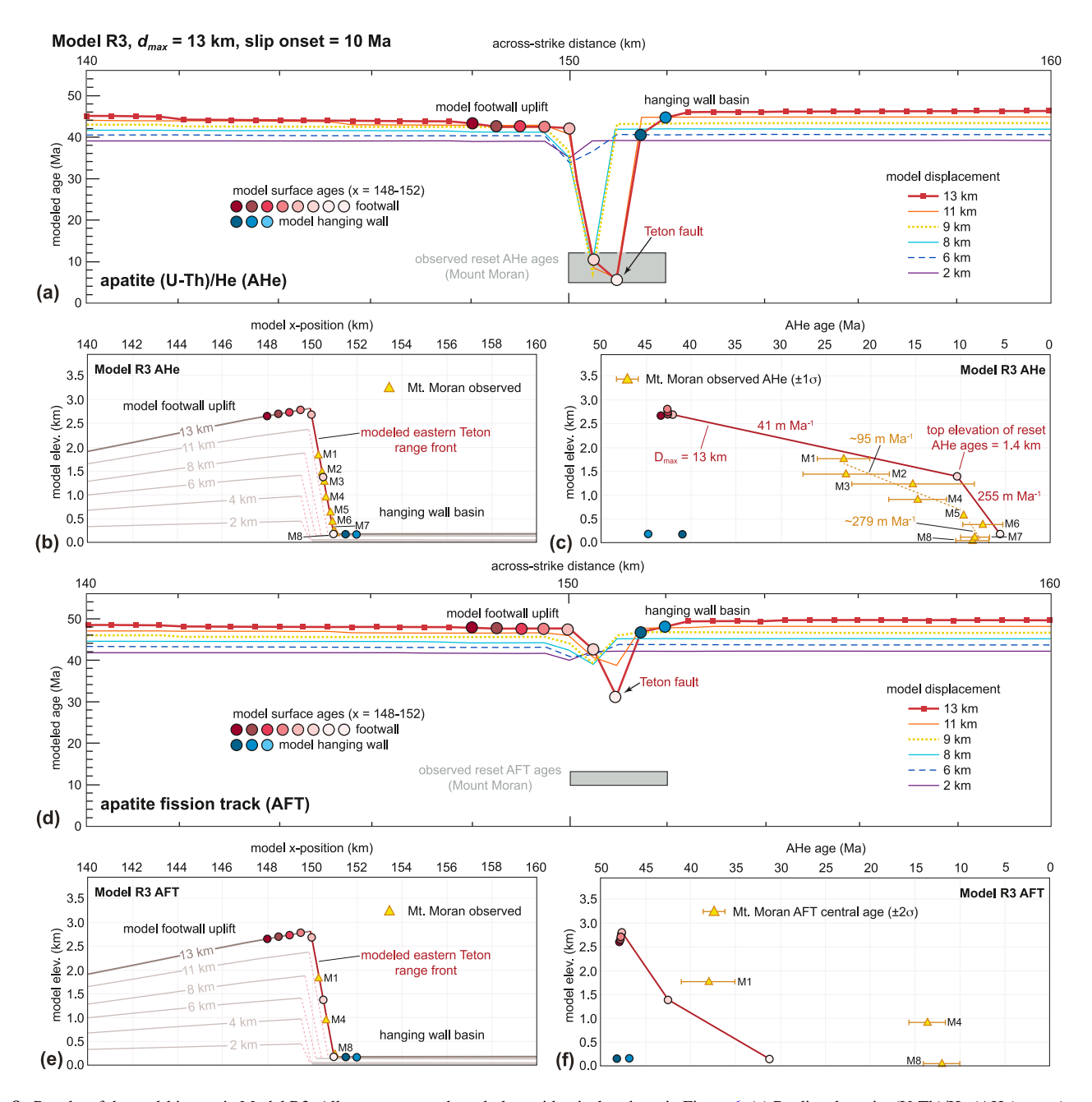


Figure 8. Results of thermal-kinematic Model R3. All parameters and symbols are identical to those in Figure 6. (a) Predicted apatite (U-Th)/He (AHe) ages (*y*-axis) at the model surface for selected displacement increments from model *x*-positions 140–160 km (*x*-axis). (b) Diagram of model *x*-position and model elevation showing the location the modeled Teton range front at the displacement intervals shown in panel (a). Colored circles correspond to the same colors in panels (a)–(f). (c) Elevation-AHe age plot. The two elevation-age relationships slopes (red line) are interpreted to highlight the upper unreset AHe ages (41 m Ma⁻¹) and the 10 Ma-recent fault motion (255 m Ma⁻¹) discussed in the main text. (d) Predicted apatite fission track (AFT) ages at the model surface for the same *x*-positions shown in panel (a). (e) Diagram of model *x*-position and model elevation showing the relative positions of modeled and observed AFT ages. (f) Elevation-AFT age plot comparing modeled and observed AFT ages. Points at the modeled Mount Moran summit and those on the eastern range front representing the Teton fault are linked by a similar red line as (c).

in the bulk temperature increase at depth between the initial steady-state geotherm and the final model step (Figure 12c). This advection also drives an increase in the near surface geotherm (max. \sim 33°C km⁻¹ in Model R7, x-position geotherm 152, Figure 12d) for the crust below the elevation of the hanging wall surface. Importantly, this range in geothermal gradient from initial to final model conditions (27–33°C km⁻¹) is consistent with the range of possible gradients indicated by models of Thigpen et al. (2021) that were constrained by surface heat flow measurements of Blackwell and Richards (2004) in the northern Teton Range. The second transient

HELFRICH ET AL. 15 of 29

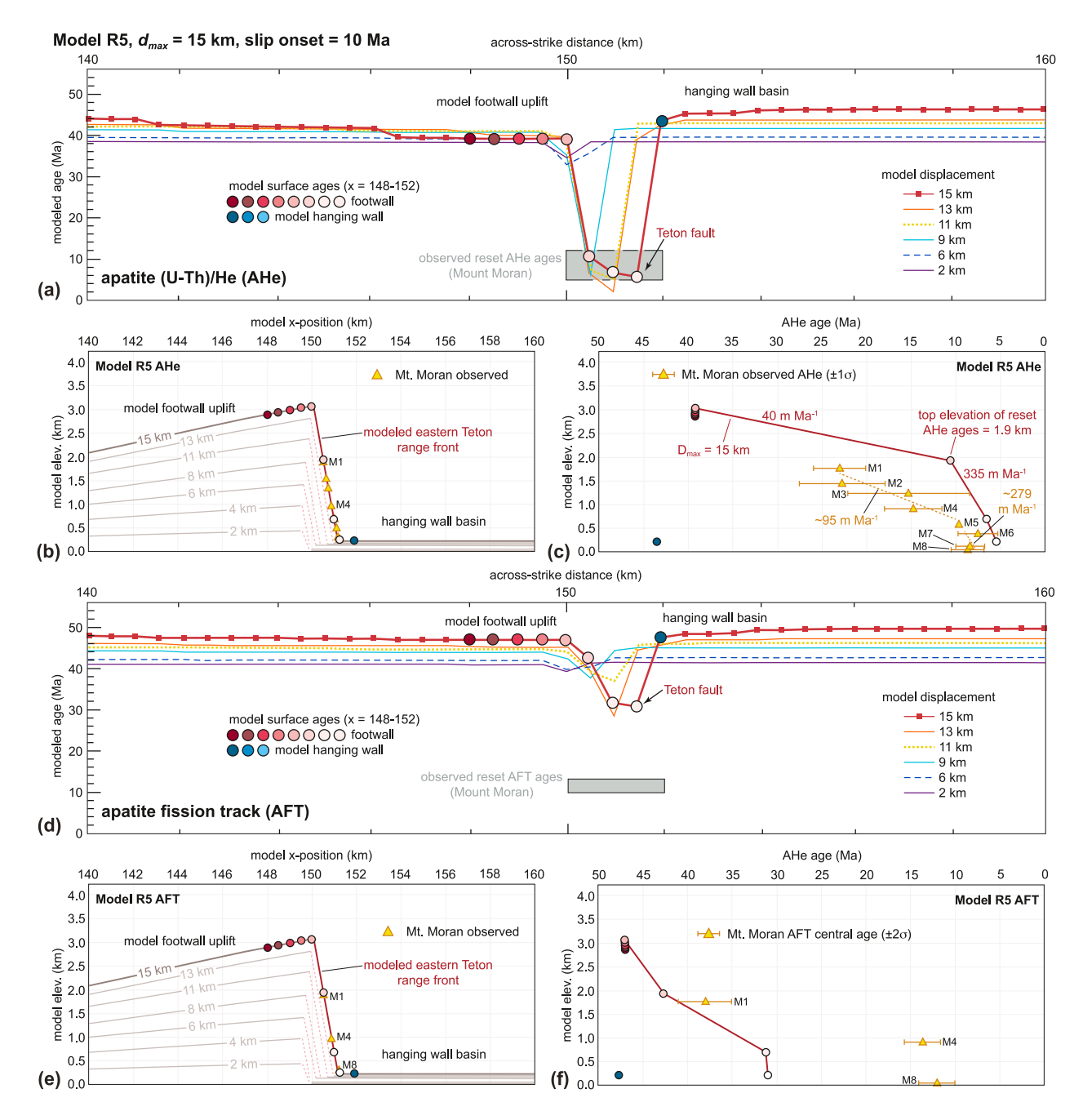


Figure 9. Results of thermal-kinematic Model R5. All parameters and symbols are identical to those in Figure 6. (a) Predicted apatite (U-Th)/He (AHe) ages (*y*-axis) at the model surface for selected displacement increments from model *x*-positions 140–160 km (*x*-axis). (b) Diagram of model *x*-position and model elevation showing the location the modeled Teton range front at the displacement intervals shown in panel (a). Colored circles correspond to the same colors in panels (a)–(f). (c) Elevation-AHe age plot. The two elevation-age relationships slopes (red line) are interpreted to highlight the upper unreset AHe ages (40 m Ma⁻¹) and the 10 Ma-recent fault motion (335 m Ma⁻¹) discussed in the main text. (d) Predicted apatite fission track (AFT) ages at the model surface for the same *x*-positions shown in panel (a). (e) Diagram of model *x*-position and model elevation showing the relative positions of modeled and observed AFT ages. (f) Elevation-AFT age plot comparing modeled and observed AFT ages. Points at the modeled Mount Moran summit and those on the eastern range front representing the Teton fault are linked by a similar red line as (c).

modification of the geotherm occurs in the higher elevation footwall that represents the uplifting range front (including the footwall AHe + AFT transect). There, a significant reduction in geothermal gradient occurs due to lateral and upward heat conduction during footwall exhumation (min. $\sim 12^{\circ}$ C km⁻¹, Figure 12d).

HELFRICH ET AL. 16 of 29



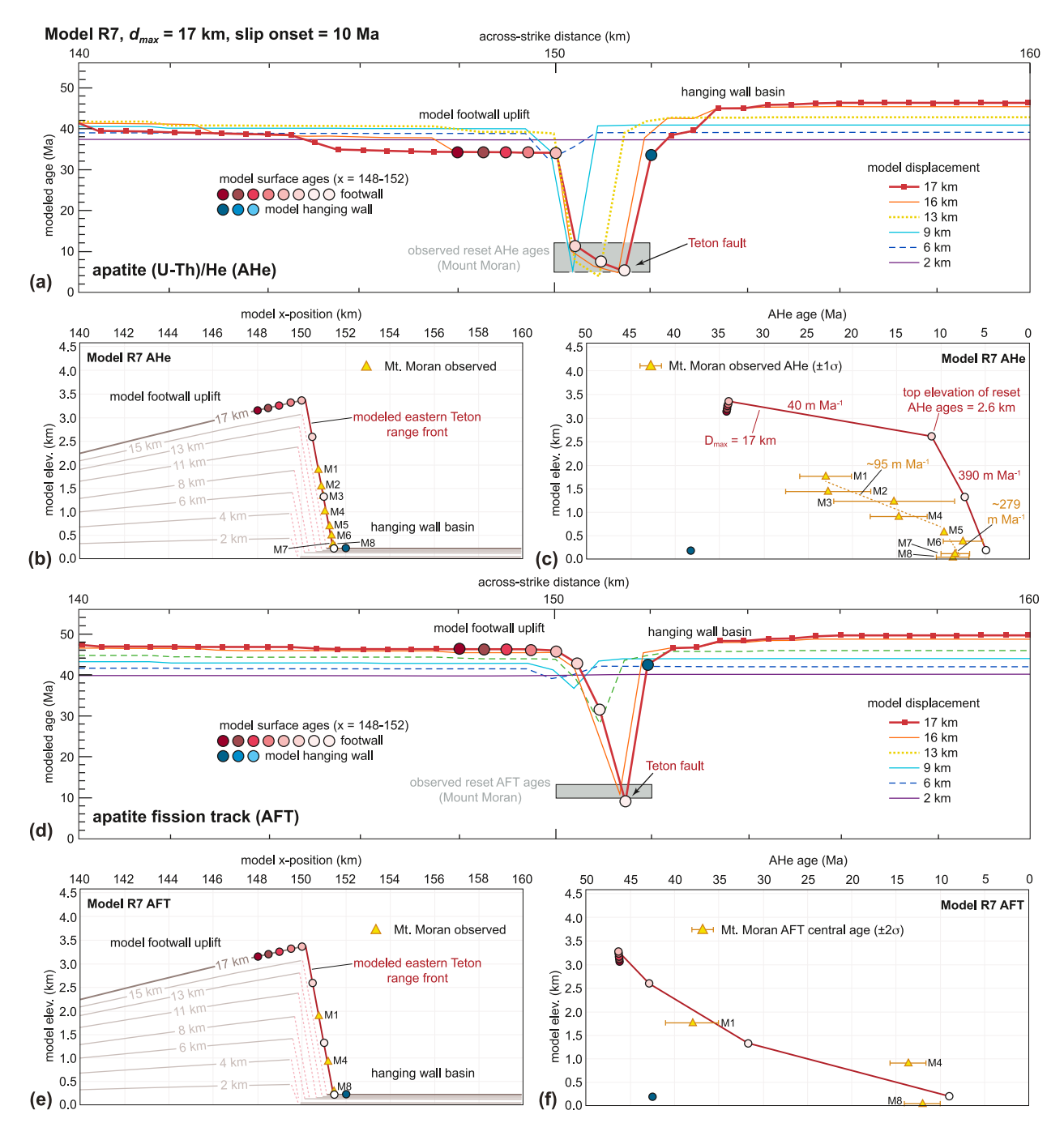


Figure 10. Results of thermal-kinematic Model R7. All parameters and symbols are identical to those in Figure 6. (a) Predicted apatite (U-Th)/He (AHe) ages (*y*-axis) at the model surface for selected displacement increments from model *x*-positions 140–160 km (*x*-axis). (b) Diagram of model *x*-position and model elevation showing the location the modeled Teton range front at the displacement intervals shown in panel (a). Colored circles correspond to the same colors in panels (a)–(f). (c) Elevation-AHe age plot. The two elevation-age relationships slopes (red line) are interpreted to highlight the upper unreset AHe ages (40 m Ma⁻¹) and the 10 Ma-recent fault motion (390 m Ma⁻¹) discussed in the main text. (d) Predicted apatite fission track (AFT) ages at the model surface for the same *x*-positions shown in panel (a). (e) Diagram of model *x*-position and model elevation showing the relative positions of modeled and observed AFT ages. (f) Elevation-AFT age plot comparing modeled and observed AFT ages. Points at the modeled Mount Moran summit and those on the eastern range front representing the Teton fault are linked by a similar red line as (c).

In the constant displacement models (R1, R2, R3, R5, and R7), AHe ages in the vicinity of the footwall uplift (~150 km across-strike distance in model space) generally evolve from older unreset values to younger reset values as displacement increases and the footwall is uplifted and exhumed. For the first three displacement

HELFRICH ET AL. 17 of 29



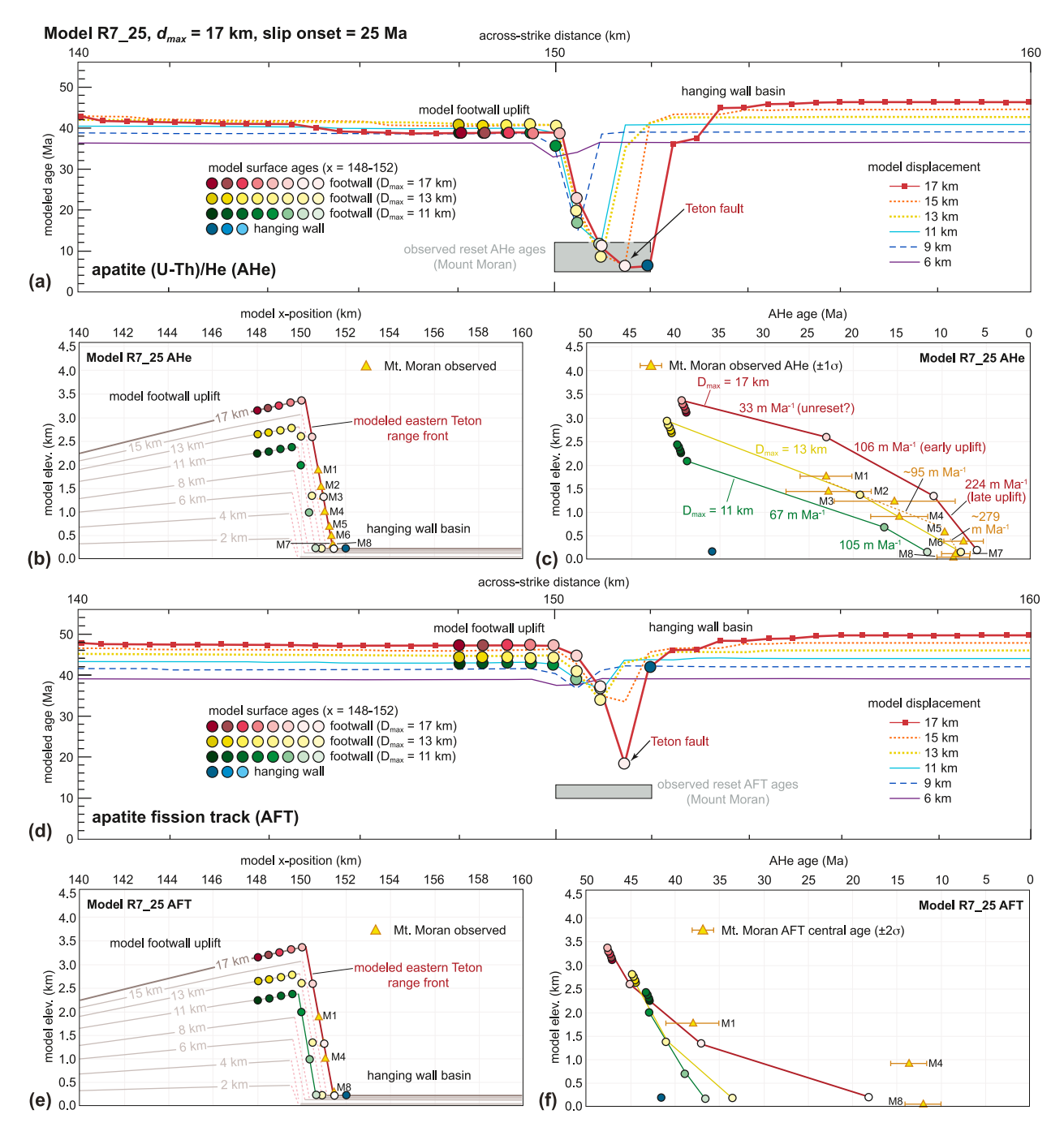


Figure 11. Results of thermal-kinematic Model R7_25. Most parameters and symbols are identical to those in Figure 6. (a) Predicted apatite (U-Th)/He (AHe) ages (y-axis) at the model surface for selected displacement increments from model x-positions 140-160 km (x-axis). The three different color circle gradations represent the x-positions of 148.0-152.0 km for $D_{max} = 17 \text{ km}$ (red to light pink), 13 km (dark to light yellow), and 11 km (dark to light green). Colored circles correspond to the same colors in panels (a-f). (c) Elevation-AHe age plot comparing modeled (colored circles) and observed (yellow triangles with 1s uncertainties) ages. The three elevationage relationship slopes for $D_{max} = 17 \text{ km}$ (red line) are interpreted to highlight the upper unreset AHe ages (33 m Ma^{-1}) and the two phases of fault motion (106 m Ma^{-1} , 224 m Ma^{-1}) discussed in the main text. (e) Diagram of model x-position and model elevation showing the relative positions of modeled and observed apatite fission track (AFT) ages. (f) Elevation-AFT age plot comparing modeled and observed AFT ages. Points at the modeled Mount Moran summit and those on the eastern range front representing the Teton fault are linked by a similar red, yellow, and green lines as (c).

increments (2, 4, and 6 km), all models yield either completely unreset (>38 Ma) or partially reset (>32 Ma) AHe ages at the model surface (Figures 6a–6c, 7a–7c, 8a–8c, 9a–9c, 10a–10c, and 11a–11c). These AHe ages represent footwall particles that were completely unreset ($T < T_c$) when the model starts at 48 Ma and are unroofed during initial footwall uplift.

HELFRICH ET AL. 18 of 29

M7-8-07

M8-8-32

Base

2,185

2,116

2,064

Table 4

Thermal-Kinematic Model Variants and Summaries of Model Predicted AHe and Apatite Fission Track (AFT) Ages and Average AHe and Central AFT Ages From Mount Moran Transect of Brown et al. (2017) and Thigpen et al. (2021)

Mount Moran Transect of Brown et al. (2017) and Thigpen et al. (2021)										
Model	$D_{\rm max}$ (km)	<i>X</i> -position (km)	Model elev. (m)	AHe age (Ma)	Elevation-AHe age-slope (m/Ma)	Unreset versus reset slope (AH	e) AFT age (Ma) –		
Model ag	ges									
R1	9	150.0	1,474	39.6			47.0	_		
		150.5	118	8.9	44	Unreset	42.1	-		
R2	11	150.0	2,073	42.1			47.6	_		
		150.5	686	9.5	43	Unreset	42.2	_		
		151.0	152	7.1	223	Reset	40.2	_		
R3	13	150.0	2,684	42.2			47.7	-		
		150.5	1,382	10.3	41	Unreset	42.5	-		
		151.0	168	5.6	255	Reset	31.3	_		
R5	15	150.0	3,067	39.2			47.1	_		
		150.5	1,932	10.6	40	Unreset	42.6	-		
		151.0	689	6.6			31.2	_		
		151.5	219	5.5	335	Reset	30.9	-		
R7	17	150.0	3,373	34.0			46.3	_		
		150.5	2,605	11.1	34	Unreset	42.8	_		
		151.0	1,334	7.3			31.6	_		
		151.5	202	4.9	390	Reset	8.9	_		
R7_25	17	150.0	3,373	46.2			50.1	_		
		150.5	2,605	22.9	33	Unreset	44.9	_		
		151.0	1,334	10.9			37.0	_		
		151.5	202	5.8	224	Reset	18.1	_		
					Elevation-AHe age-slope					
Sample	Elev. (m) Model elev. (m)	AHe age (Ma)	Error (Ma)	(m/Ma) U	nreset versus reset slope (AHe)	AFT age (Ma)	Error		
Mt. Mora	an Observed	Ages								
M1-8-	15 3,835	1,771	23.0	2.9			35.0	3.1		
M2-8-3	30 3,505	1,441	22.8	4.8						
M3-8-3	31 3,304	1,240	15.3	6.8						
M4-8-0		911	14.8	3.2	95	Unreset	13.6	2.0		
M5-8-0		572	11.9	1.0						
M6-8-0		386	7.5	2.2						
1,10 0-0	2,730	300	7.5	2.2						

Note. Model results derived from surface nodes at *x*-positions of 150.0–151.5 representing the modeled Mount Moran transect. Nodal positions and nodes used for unreset and reset AHe slope calculations are shown in Figures 6–11. Unreset and reset slope calculation methodology for model-derived AHe ages is explained in the main text. Unreset and reset slope are not calculated for AFT data, as most model-derived points yield AFT ages indicative of partial annealing. Elevation values for observed samples = actual elevations. Elevation values for observed data modified to be equivalent to model elevations by subtracting the base elevation value of 2,064 m from the observed elevation. Unreset and reset slopes for the observed AHe data derived from Thigpen et al. (2021).

279

10.1

8.7

1.6

1.8

121

52

After \sim 8 km of total displacement, all models yield two AHe age populations; the older sample population has continued to rise in elevation with continued uplift, but the magnitude of footwall uplift and subsequent exhumation results in reset (<10 Ma) model AHe ages at lower elevation at or near the base of the modeled footwall (Figures 6c-11c). These reset points were derived from model depths with $T > T_c$ at the model start time. With increasing displacement magnitude, these relatively young ages are translated to higher and higher elevations via footwall uplift. In addition, new lower elevation points are brought to the surface that, predictably, record

Reset

11.7

1.7

HELFRICH ET AL. 19 of 29

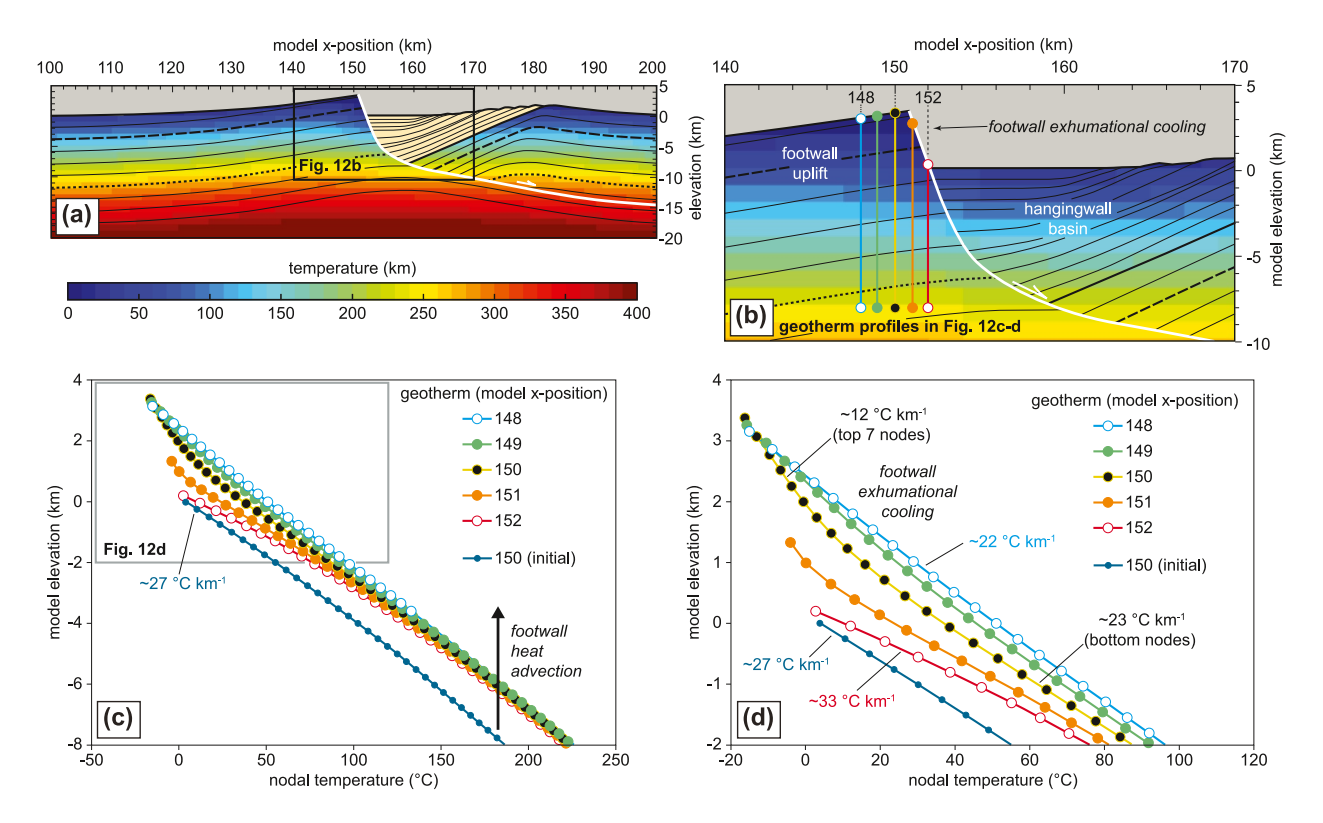


Figure 12. Evaluation of model-derived geothermal gradients predicted for the footwall uplift zone. (a) Thermal field for final model step ($D_{max} = 17$ km) for Model R7. Location of (b) inset shown. (b) Zoomed inset of model region at the faulted transition from footwall uplift to hanging wall basin. Geotherm profiles shown in panels (c) and (d) are indicated. (c) Model geotherms at *x*-positions of 148, 149, 150, 151, and 152 km to a depth of 8 km for the final step of Model R7. The initial geotherm prior to the onset of fault displacement at *x*-position 150 km is also shown. The bulk upward shift in the footwall geotherms from model start to finish results from heat advection in the uplifting footwall. (d) In the highest elevation parts of the footwall, geotherm shape varies as function of *x*-position due to the interplay between bulk footwall uplift/advection and exhumational cooling. Bulk surface-directed heat advection drives near-surface compression of the isotherms and elevation of the geothermal gradient, which is highlighted by the near surface geothermal gradient of $\sim 33^{\circ}$ C km⁻¹ at an *x*-position of 152 km. In the higher elevation parts of the model footwall, lateral and vertical cooling of the uplifted range reduces the geothermal gradient as low as ~ 12 C° km⁻¹ near the modeled range top at *x*-position 150 km.

progressively younger ages. This younging of the lower elevation points as displacement increases yields an elevation-AHe age gradient with younger ages at lower elevation progressing to older ages at higher elevation, as generally predicted in thermochronologic studies of normal faults (e.g., Ehlers, 2005).

In these models, emphasis is placed on evaluating three key results. First, the threshold amount of exhumation required to uplift and exhume fully reset (i.e., ≤ 10 Ma) AHe and AFT ages in the model footwall produces a minimum displacement constraint for the Teton fault, as fully reset ages are observed in the Teton fault footwall. Next, it is important to note the maximum elevation of any reset AHe and AFT ages, as this can be a key indicator of the total uplift the footwall has experienced after bringing those reset ages to the surface. Lastly, the different slopes in the elevation-AHe age plots (Figures 6–11c) can highlight changes such as the onset of uplift (and faulting) as well as the slip rate, as higher slip rates should theoretically yield higher values for the elevation-age relationship. All three of these model characteristics can be directly compared with the same characteristics from the observed data along the Mount Moran transect, which is summarized in Table 4. Because the Moran transect only includes three observed AFT dates and none of them yield fully reset central ages (i.e., ≤ 10 Ma), we did not calculate elevation-age slopes for the AFT data.

In Model R1 ($D_{max} = 9$ km, 0.9 km Ma⁻¹), one AHe age ~ 8.9 Ma is predicted along the base of the modeled footwall after a displacement of 9 km (Figures 6a–6c). Because of the grid resolution used in the thermal-kinematic models (500 m \times 500 m), 2–4 cooling ages can be extracted along the modeled transect for each time step, depending on the total relief. In Model R2 ($D_{max} = 11$ km, 1.1 km Ma⁻¹) two reset AHe ages of ~ 9.5 Ma and ~ 7.1 Ma are recognized after 11 km of displacement, with the highest reset age lying ~ 0.7 km above the valley floor (Figures 7a–7c). For reference, the modeled valley floor lies at a datum elevation of 0.0 km. At a D_{max} of 13 km, Model R3 (~ 1.3 km Ma⁻¹) yields reset AHe ages of ~ 10.3 and ~ 5.6 Ma in the footwall at

HELFRICH ET AL. 20 of 29



elevations of ~1.4 and ~0.2 km above the valley floor (Figures 8a–8c). Like Models R1 and R2, Model R3 only yields reset AHe ages at the surface once the 8 km displacement threshold is reached. At a D_{max} of 15 km in Model R5 (1.5 km Ma⁻¹), reset AHe ages (~9.5 Ma) are predicted as high as ~1.9 km above the valley floor (Figures 9a–9c). At a D_{max} of 17 km in Model R7 (1.7 km Ma⁻¹), a reset AHe age of 11.1 Ma is predicted at an elevation of ~2.6 km above the valley floor (Figures 10a–10c). Although the modeled age point is technically older than the reset age cut-off of ~10 Ma specified above, these higher elevation points would have been below this cut-off when initially exhumed but have increased in age as the footwall continued to uplift to the end of model time.

The AHe age-elevation gradients for the constant displacement models all show two elevation-AHe age slopes; a relatively low slope (40–44 m Ma^{-1}) composed of older unreset ages at higher elevation and a relatively steep slope composed younger reset ages at lower elevation. The higher elevation slope reflects the "unreset" overburden, which has a thickness that is controlled by the depth to T_c (i.e., deeper T_c = thicker overburden sequence). The depth to T_c is, in turn, controlled by the initial prescribed geothermal gradient. Because the initial geothermal gradient is the same for all models, this unreset overburden age-elevation slope is generally consistent across all models (40–44 m Ma^{-1} ; Figures 6c–11c). The steeper slope at lower elevations in each model represents the age-elevation gradient produced for points that are progressively exhumed from depths initially deeper than T_c . Because these points were reset prior to uplift, the elevation-AHe age slope reflects the rate of footwall uplift, with increasing uplift rate corresponding to higher displacement rates. These slopes range from 223 to 390 m Ma^{-1} , with the higher values corresponding to models with higher maximum displacements and thus faster average slip rates for the same ~ 10 Ma displacement time (Figures 6c–11c).

In all models, AFT ages were also tracked for comparison with AFT central ages of Brown et al. (2017) from the Moran transect. In the constant displacement models, AFT ages show a similar evolution to the modeled AHe ages, wherein AFT ages in the footwall adjacent to the modeled Teton fault gradually decrease in age as displacement is accumulated and exhumation progresses (Figures 6d–6f, 7d–7f, 8d–8f, 9d–9f, 10d–10f, and 11d–11f). This progressive decrease in AFT ages reflects exhumation of model points from depths where temperatures are hot enough to drive partial AFT annealing (120–60°C; Green et al., 1989; Laslett et al., 1994). In constant displacement Models R1 ($D_{max} = 9 \text{ km}$) and R2 ($D_{max} = 11 \text{ km}$), AFT ages in the modeled footwall <0.2 km above the valley floor are ~42.1 Ma (Figures 6e and 6f) and ~40.2 Ma (Figures 7e and 7f), respectively, at the end of the model run. In Models R3 ($D_{max} = 13 \text{ km}$) and R5 ($D_{max} = 15 \text{ km}$), points with partially reset AFT ages ranging from 31.3 to 10.9 Ma are predicted for the model footwall (Figures 8e–8f and 9e–9f) at the end of the model run. Of the constant displacement models, only R7 ($D_{max} = 17 \text{ km}$) produces enough footwall uplift and erosion to exhume completely reset AFT ages of ~11.0 Ma and ~8.9 Ma after displacements of 16 and 17 km, respectively. These reset ages are predicted at ~0.2 km above the modeled valley floor (Figures 10e and 10f).

4.2.2. Early (25 Ma) Slip Onset (Model R7_25)

Model R7_25 was run to examine a potential earlier transient cooling scenario for the Moran transect as indicated by inverse thermal history modeling of Thigpen et al. (2021, their Figure 4a). In that model, the expected thermal history for the lowest elevation sample (M8) includes an initial cooling pulse from 25 to 18 Ma followed by an accelerated cooling pulse from \sim 10 Ma to present. In the model presented here, this potential cooling scenario is implemented with 4 km of displacement at a constant rate (\sim 0.7 km Ma⁻¹) from 25 to 19 Ma and a second pulse involving an additional 11 km of displacement at an accelerated constant rate (\sim 1.1 km Ma⁻¹) from 10 to 0 Ma.

In Model R2_25, reset ages for both the AHe and AFT systems are identified as those younger than the onset of slip at \sim 25 Ma. Like the constant slip models, Model R2_25 yields no reset AHe ages in the footwall until at least 8 km of displacement has been accumulated (Figure 11a). For the 8 and 9 km displacement increments, the lower elevation parts of the model footwall yield predicted AHe ages of 18.5 Ma and 14.8 Ma, respectively, with both points located near the base of the transect at the valley floor. As displacement increases, the AHe ages at the base of the modeled transect become progressively younger and the reset AHe ages reach progressively higher elevations (Figures 11b and 11c). For displacement magnitudes of 11–13 km, the model AHe ages define two elevation-age slopes along the footwall transect, including a relatively low slope (\sim 67 m Ma $^{-1}$) at higher elevations and a slightly steeper slope (\sim 105 m Ma $^{-1}$) at lower elevations. At displacement magnitudes >14 km, the model yields three AHe age-elevation slopes that presumably represent the pre-fault period and the two pulses of fault slip, respectively. At 17 km of displacement, these age-elevation gradients are 33 m Ma $^{-1}$, 106 m Ma $^{-1}$, and 224 m Ma $^{-1}$ (Figures 11b and 11c).

HELFRICH ET AL. 21 of 29



AFT ages in the modeled footwall yield a similar evolution to those in constant displacement Model R7, wherein relatively young AFT ages that pre-date fault motion (>25 Ma) are only observed once a displacement magnitude of 16 km is reached. At those displacements of 16 and 17 km in Model R2_25, reset AFT systems in the model footwall yield predicted ages of 19.7 Ma and 18.1 Ma (Figures 11d–11f), respectively. Both points are at a model elevation of ~0.2 km above the valley floor.

5. Discussion

5.1. Flexural-Kinematic Model Constraints on Teton Fault Displacement

The model results presented here provide multiple constraints for Teton fault displacement magnitude. First, the modeled flexural response to normal faulting can be used to eliminate displacement scenarios that cannot reproduce critical aspects of the modern Teton system. In particular, any viable displacement solution must yield a footwall uplift magnitude sufficient to generate both the ~1.8 km of modern relief on the eastern range front at Mount Moran and the required >2.0 km of erosion indicated by the estimated thickness of missing Paleozoic-Quaternary stratigraphy above Mount Moran (e.g., Christiansen et al., 1978; Love et al., 1992). In our models, total footwall uplift is an isostatic response to both crustal extension and erosion of the uplifted footwall block and is equivalent to the sum of eastern range front relief and the eroded thickness of the footwall block (Figure 2a).

In the flexural-kinematic Model 13, a total footwall uplift magnitude of \sim 1.8 km, equivalent to the modern relief, is reached at a displacement magnitude of 6 km (Figure 4b). Because the total erosion of \sim 2.1 km is equally distributed across each of the displacement increments, \sim 13 km of displacement is required to produce a total footwall uplift magnitude of \sim 3.9 km (Figure 4f), equivalent to the >3.8 km required from observations. In the same model, displacement magnitudes of 9 and 11 km yield footwall uplift magnitudes of 2.7 and 3.3 km, respectively, although these uplift magnitudes could be marginally increased if the entire >2.0 km of footwall erosion had occurred by the time the model reaches these displacement increments. In the current flexural-kinematic model, displacement magnitudes of 9 and 11 km are only prescribed to have eroded 0.9 and 1.1 km of footwall stratigraphic thickness, respectively. Despite these complexities, the results of Model 13 indicate that Teton fault displacement must be significantly greater than 6 km and could potentially be as high as 13+ km.

5.2. Thermal-Kinematic Model Constraints on Teton Fault Displacement

Comparisons between the observed AHe and AFT data and the results of the thermal-kinematic models presented here provide further constraints on Teton fault displacement. In the thermal-kinematic models the predicted cooling ages are controlled by a combination of particle motions as prescribed by the flexural-kinematic model, the rate and magnitude of footwall block exhumation, and the transient thermal evolution of the crust. In these models, isotherm geometry is modified by surface-directed heat advection due to uplift in the model footwall and downward deflection of isotherms in the hanging wall due to sedimentation and burial of relatively cold material in the model basin.

In the Teton-Yellowstone system, migration of the Yellowstone supercaldera into its present position imparts additional complexities to the thermal state of the crust and the present-day (and paleo-) isotherm geometry. To address this, Thigpen et al. (2021) developed multiple 1-D thermal models to estimate along strike variation in geothermal gradient beneath the Teton Range. In those models, which were constrained by measured surface heat flow values of Blackwell and Richards (2004), the possible range of upper crustal geothermal gradients were calculated for a range of representative crustal thermal parameters (e.g., radiogenic heat production, thermal conductivity, basal mantle heat flux). Near Mount Moran, those models yield a modern upper crustal geothermal gradient of $26-29^{\circ}$ C km⁻¹ for surface heat flow values of \sim 0.087 W m⁻² (Blackwell & Richards, 2004). These calculations highlight that despite the proximity of the Yellowstone hotspot to the modern Teton range, geothermal gradient values are not predicted to be anomalously high. The thermal-kinematic models presented here yield an initial upper crustal thermal gradient of \sim 27°C km and a final gradient of 27–33°C km⁻¹ for the upper crust beneath the modeled footwall at the end of the model run (Figure 12).

If the geothermal gradient generally represents the crustal heat flow conditions in the upper 5 km of Teton crust, then integration of the thermal-kinematic and flexural-kinematic models with the thermochronology data provides critical constraints for Teton fault evolution. As a reminder, for the comparison between the observed and modeled AHe and AFT systems, we are primarily interested in: (a) the AHe and AFT ages of samples exhumed

HELFRICH ET AL. 22 of 29



along the footwall transect, (b) the elevation-AHe age slopes along the footwall transect, and (c) the highest elevation of reset AHe samples along the footwall transect, which is influenced primarily by footwall uplift magnitude. To enable better direct comparison between the models and the observed transect values for (c), the approximate elevation of the Jackson Hole valley floor was subtracted from the elevation at which each sample was collected, to make the elevation of the AHe and AFT samples above the valley floor equivalent to the model derived points, which has a datum value of 0 m at the valley floor. For example, the valley floor elevation at the base of the Moran transect is \sim 2.06 km, so this is subtracted from the elevation reported for each transect sample in Brown et al. (2017). As a reminder, the thermal field in the model is initiated at 48 Ma and fault slip in the constant displacement model begins at \sim 10 Ma. In the variable displacement model, fault slip begins at 25 Ma and accelerates at 10 Ma.

Along the Mount Moran transect, AHe data of Brown et al. (2017) and Thigpen et al. (2021) define a high-elevation elevation-AHe age slope of 95 \pm 13 m Ma⁻¹ (Figure 6c). Additionally, a second age-elevation gradient of 279 m Ma⁻¹ was calculated using a projection from the highest elevation reset Moran transect sample to an inferred depth of the AHe T_c , interpreted as the 0 Ma age (Figure 6c; Thigpen et al., 2021, their Figure 6d). The inflection point between the two elevation-AHe age slopes, which is generally interpreted as the time of footwall uplift onset due to fault slip at Mount Moran, is ~10 Ma. Along the Mount Moran transect, reset AHe ages are observed as high as 0.5 km above the valley floor.

In the constant displacement thermal-kinematic models presented here, all models yield an elevation-AHe age slope of 40-44 m Ma⁻¹ for the higher elevation parts of the transect and then steeper elevation-AHe age slopes ranging from 223 to 390 m Ma^{-1} for D_{max} scenarios from 11 to 17 km (Models R2, R3, R5, and R7; Figures 6c– 10c). For the 9 km D_{max} scenario (Model R1; Figure 6c), the magnitude of footwall uplift and subsequent exhumation is below the threshold to exhume the steeper elevation-age slope that reflects 10 Ma-recent active fault slip. Model R2, with a D_{max} of 11 km, yields a low elevation slope of 223 m Ma⁻¹, slightly lower than that observed along the Moran transect. However, the top elevation of reset samples in the model is ~0.7 km (Figure 7c), close to value of \sim 0.5 km at Mount Moran. Models R3 and R5, which have D_{max} values of 13 and 15 km, yield reset elevation-AHe slopes of 255 m Ma⁻¹ and 335 m Ma⁻¹, respectively, that bracket the observed reset elevation-AHe age slope observed at Moran. In the R3 model, the highest elevation reset samples occur at ~1.4 km above the valley floor (Figure 8c), which is just on the high end of the observed values, whilst the reset samples in the R5 model occur at a considerably higher elevation above the valley floor (~1.9 km, Figure 9c). The lower elevation-AHe age slope of 390 m $\mathrm{Ma^{-1}}$ for Model R7 ($D_{max} = 17$ km; Figure 10c) is considerably higher than the observed gradient at Mount Moran. Combined, these models indicate that, for a fault slip onset of ~ 10 Ma and slip at a constant rate, modeled D_{max} values of 11–13 km appear to be most consistent with the observed AHe values along the Moran transect.

Comparisons between the observed and predicted AFT data in the constant displacement models are generally less diagnostic of a particular D_{max} value but may yield important insights for a more complex structural evolution. Along the Moran transect, three AFT samples of Brown et al. (2017) for the upper, middle, and lower parts of the Moran transect yield central ages 38.0 ± 3.1 M, 13.6 ± 2.0 Ma, and 11.7 ± 1.7 Ma, respectively. A fourth AFT sample from Moran Bay on the North flank of Mount Moran yields a central age of 9.5 ± 1.4 Ma. Like the AHe data, the sample elevations have been adjusted to allow direct comparison with the modeled AFT ages (Figures 6f–10f). In Models R1 and R2, the magnitude of uplift and erosion is not sufficient to exhume partially reset AFT ages (Figures 6f and 7f). Models R3 and R5 yield partially reset (\sim 30 Ma) AFT ages at maximum elevations of \sim 0.8 km above the modeled valley floor (Figures 8f and 9f). Of the constant displacement models, only Model R7 km yields completely reset AFT ages of \sim 10 Ma that can compare favorably with the observed AFT ages at low elevations along the Moran transect. In that model, these ages only occur at displacement magnitudes of 16 and 17 km (Figure 10f), which are significantly higher D_{max} values than those indicated by the AHe data.

In the R7_25 Model, the highest D_{max} threshold of 17 km yields three elevation-AHe age slopes interpreted to reflect: (a) exhumation of the unreset or partially reset pre-uplift material above the T_c depth (b) the early uplift pulse at ~25 Ma, and (c) the late (10 Ma-recent) rapid uplift pulse (Figure 11c). Although we would expect something approximating these three elevation-age slopes to exist for lower displacement thresholds in this model, the highest elevation-AHe age slope value of ~224 m Ma^{-1} representing the late uplift pulse predicted at a D_{max} of 17 km is not apparent in the lower displacement models. However, we interpret that lower Dmax values of

HELFRICH ET AL. 23 of 29



this scenario simply didn't produce a threshold amount of footwall uplift and exhumation to expose material reflecting this late and fast pulse of uplift, as the total exhumation (and the exhumation from 10 Ma to recent) is lower in the lower D_{max} models (Figure 11c). We expect that, given sufficient continuing uplift and exhumation, a relatively high elevation-AHe age slope reflecting the final fault motion pulse would reach the surface at the base of the model transect. Despite the modeling caveat mentioned above, the predicted AHe age trends show the best match to the observed data at a D_{max} value of 13–14 km, and displacement magnitudes as low as 11 km yield predicted AHe ages that are within error of many of the observed ages (Figure 11c). Like the constant displacement models, modeled AFT ages for the R7_25 Model generally yield poor fits with the observed AFT central ages. In this model, only displacement magnitudes of 16 and 17 km yield reset ages of ~18 and ~20 Ma at low elevations (Figure 11f). However, this model does yield a fit to the observed AHe data at D_{max} values of 13–14 km (potentially up to 16 km) without the necessity of producing the relatively steep elevation-AHe slopes (335–390 mm Ma⁻¹) that are significantly higher than the observed data in the lower elevation parts of Teton Range (~279 m Ma⁻¹). Thus, despite not providing a perfect match to the observed data, the multiphase uplift and cooling history in Model R7_25 may indicate that the uplift and cooling history of the Teton Range is potentially more complex than is considered in the constant displacement models.

5.3. Developing a Unified Interpretation for Maximum Teton Fault Displacement

The large range of previous Teton fault displacement estimates (2.1–12.6 km) and slip onset ages of (2–28 Ma; Table 1) can, at least partially, be attributed to the diversity of techniques and evidence used to constrain interpretations. These include: (a) those that are derived from geophysical data, (b) those that are derived from stratigraphic cut-offs or rotation of hanging wall stratigraphy and (c) those that are derived from uplift and cooling studies. Below, we consider these displacement (and fault timing) estimates in the context of our model results.

As mentioned above, integration of thermal-kinematic models and observed AHe data appear to require that Teton D_{max} values lie between 11 and 13 km for constant displacement models with slip onset at ~10 Ma (Models R2 and R3), or potentially as high as 16 km if slip is initiated at ~25 Ma (Model R7_25). Mapping studies (e.g., Love, 1977, 1987; Love & Reed, 1971) that rely on extrapolated cut-offs of the Precambrian-Paleozoic unconformity in the hanging wall basin yield Teton D_{max} estimates of 7.6-11.0 km that overlap with the lower end of these modeled D_{max} estimates. Early geophysical studies (Behrendt et al., 1968; Lavin & Bonini, 1957; Tibbetts et al., 1969) yield similar, albeit slightly lower D_{max} estimates. Those studies interpreted lower Paleozoic units overlying basement to lie at a maximum depth of 5.0-6.1 km east of Jackson Lake. By combining this depth estimate with the ~1.8 km relief at Mount Moran, those studies interpreted a maximum vertical displacement of 7-8 km for the Teton fault. However, more recent regional subsurface mapping (e.g., Blackstone, 1993; Wyoming State Geological Survey, 2022) interpreted the depth to basement in that area is to be >6.5 km. In those studies, vertical basement offset across the Teton fault near Mount Moran is estimated to be >8.5 km (28,000 ft; Wyoming Geological Survey, 2022, their Plate 1). In the flexural-kinematic models with displacements that yield the best fit to the AHe data, the hanging wall basin depth (proxy for depth to basement) yields similar results, with basin depths of \sim 6.0 km at a D_{max} of 9 km, \sim 6.7 km at a D_{max} of 11 km, \sim 7.5 km for a D_{max} of 13 km, and ~8 km for D_{max} of 15 km. This overlap between the Wyoming Geological Survey (2022) estimates and the models presented here highlights a key consistency between hanging wall basin depths determined from geophysical data and those predicted by the integration of flexural-kinematic modeling and thermal-kinematic modeling.

Despite the consistencies noted above, a number of studies have proposed Teton fault D_{max} estimates that are considerably lower. Most of these relatively low Teton D_{max} estimates are derived from rotation of the ~2.06 Ma Huckleberry Ridge (2.5–3.5 km, Byrd et al., 1994) or ~4.45 Ma Kilgore-Heise tuffs (3.8–6.7 km displacement; Gilbert et al., 1983; Smith et al., 1993) in the Teton fault hanging wall. In the thermal-kinematic models, no scenarios with D_{max} values <8 km are capable of reaching a threshold of footwall exhumation that yields reset AHe ages in the modeled footwall transects (Figure 11). In all of these models, low elevation AHe ages along the eastern base of the Teton Range are predicted to be much older (at least >20 Ma but more likely >35 Ma), depending on their prior uplift history. Importantly, Brown et al. (2017) reported reset AHe ages in low elevation positions along transects for Rendezvous Mountain, Grand Teton, and Mount Moran, as well as multiple low elevation samples between these transects. Integration of those results with our models leads us to interpret that not only should the D_{max} value at Mount Moran be >8 km, but most positions along the Teton Range front likely have experienced total displacements >8 km.

HELFRICH ET AL. 24 of 29



However, these lower D_{max} estimates derived from rotation of volcanic units and the higher D_{max} values indicated by our model results need not be mutually exclusive, as the fault displacement magnitude and timing indicated by rotation of the volcanic tuffs may fit within modeled displacement scenarios presented here. Because differential rotation of well-dated stratigraphy provides a time component, these lower D_{max} estimates generally require an explicit (or implicit) minimum age of Teton fault slip onset, which in the case of the volcanic tuffs would be significantly younger (2.0–4.5 Ma) than the ages determined by inverse thermal history models of AHe and AFT data (~10 Ma, Thigpen et al., 2021). In the R2 Model with a D_{max} of 11 km, the constant slip rate of 1.1 km Ma⁻¹ yields ~2.2. and ~4.9 km of Teton fault displacement in the final ~2 Ma and 4.45 Ma of model time, respectively. For the R3 Model with a D_{max} of 13 km, the 1.3 km Ma⁻¹ constant slip rate yields ~2.6 and 5.8 km of Teton fault displacement for the same time interval. In the case of both the R2 and R3 Models, the displacement predictions yield broadly similar results with the timing and displacement estimates indicated by the volcanic tuffs. Critically, this interpretation provides a key integration between low D_{max} /late fault onset estimates and significantly higher D_{max} estimates required to match the observed AHe data in the Teton Range.

Placing the observed AFT data of Brown et al. (2017) from Mount Moran into a unified displacement framework remains as a persistent challenge. In the constant displacement models with slip onset at ∼10 Ma, only D_{max} values of 16 and 17 km in Model R7 yield completely reset AFT ages of \sim 10 Ma that are similar to observed AFT ages at low elevations along the Moran transect, however these models yield a poor fit between modeled and observed AHe data (Figure 11e). In Model R7_25, displacements of 16 and 17 km provide a better fit between the model predicted and observed AHe data (Figure 11f), and the predicted AFT ages from these models are older (~20 Ma) than the observed ages at low elevation near Mount Moran (11-13 Ma). We interpret the results of these models as indicating that the AFT system at Mount Moran may record a more complex uplift record that, at least in part, could be unrelated to Teton normal faulting and uplift of the modern Teton Range. Complexities imparted by Laramide deformation prior to Miocene activation of the Teton fault, including motion on and/or reactivation of the Forellen Peak fault, could have affected the composite thermal history recorded in these footwall units (e.g., Lageson, 1992). This type of complexity was also recognized in the previous AFT data from the Teton Range (Roberts & Burbank, 1993), which was interpreted to indicate uplift of the basement block containing the proto-Teton Range prior to the onset of Teton fault extension. To better characterize this older uplift history, a more comprehensive study that includes more AFT samples or even employing a thermochronology technique with a higher T_c than the AFT system may be required. Unfortunately, because the study of Roberts and Burbank (1993) preceded the zeta calibration technique employed for AFT data in Brown et al. (2017), the two data sets cannot be simply integrated or even directly compared. Despite these challenges imparted by the AFT data, the consistencies between the model results presented here, the observed AHe data from Mount Moran, and the previous geophysical and mapping studies (including integration of the relatively low D_{max} estimates of multiple studies) leads us to interpret that the Teton fault in the vicinity of Mount Moran likely records a D_{max} of >8 km from Miocene to recent, with modeled D_{max} values of 11-16 km providing the best fit to the observed AHe data.

6. Conclusions

This analysis, which involves integration of flexural-kinematic and thermal-kinematic modeling with thermochronology to test evolutionary models of crustal-scale normal faults, provides critical insights for the displacement history of the Teton fault and uplift of the Teton Range. Previous studies have shown how footwall uplift in extensional systems is primarily a function of crustal flexural parameters, fault geometry and detachment depth, and displacement magnitude, and other studies have demonstrated the utility of using footwall age-elevation thermochronology gradients to deduce uplift histories. However, the integration of particle flow vectors derived from flexural-kinematic scenarios into the modified Pecube-D thermal code allows for calculation of potentially more complex particle T-t histories that result from the interplay of fault motion, isostasy, footwall erosion, and uplift-related heat advection. In our analysis, flexural-kinematic model with relatively low T_e (\sim 5 km) yield the best-fit to the flexural profile of the Teton Range and of those models, only those with D_{max} significantly >6 km can produce footwall uplift magnitudes sufficient to account for the total eroded thickness footwall overburden (2.0–2.3 km) and the preserved modern relief near Mount Moran (\sim 1.8 km). Thermal-kinematic models of these flexural scenarios with D_{max} values of 11–13 km and Teton fault displacement initiating at \sim 10 Ma provide the best fit to observed AHe data at Mount Moran. However, these models only yield relatively young AFT ages (\sim 10 Ma) observed at the base of Mount Moran in models with D_{max} values >16 km. A

HELFRICH ET AL. 25 of 29



more complex model with slip initiating at \sim 25 Ma and accelerating at \sim 10 Ma provides a relatively good fit to AHe data up to D_{max} values of 16 km, however those models yield predicted AFT ages of \sim 20 Ma near the base of Mount Moran. We interpret these complexities in the higher T_c AFT system as potentially impacted by an older and perhaps more complex uplift history for the basement block now dissected by Miocene motion on the Teton fault. Even with these complexities in the deeper thermal history noted, this example highlights the how a workflow previously applied to thrust belts can provide key constraints for evolutionary models of complex and potentially controversial extensional structural systems.

Data Availability Statement

All thermochronology data discussed in this study are derived from Brown et al. (2017) and Thigpen et al. (2021) and are also reported in the supplementary material (Tables S1 and S2 in Supporting Information S1). Flexural-kinematic models were completed using an academic license of the commercial ©*Move* software at the University of Pittsburgh. Thermal-kinematic models were completed using the open-source *Pecube-D* software (Ehlers, 2023) from the Earth System Dynamics Research Group at the Universitat Tübingen.

Acknowledgments References

This work was supported by a UW-NPS Grant and NSF-EAR 1932808 to JRT and a GSA Student Research Grant to ALH. NAD gratefully acknowledges Petroleum Experts for the academic license of Move at the University of Pittsburgh. Review comments by Maggie Curry, an anonymous reviewer, and associate editor Eva Enkelmann significantly improved a previous version of this manuscript.

Allmendinger, R. W., Hauge, T. A., Hauser, E. C., Potter, C. J., Klemperer, S. L., Nelson, K. D., et al. (1987a). Overview of the COCORP 40°N Transect, western United States: The fabric of an orogenic belt. *GSA Bulletin*, 98(3), 308–319. https://doi.org/10.1130/0016-7606(1987) 98<308:ootcnt>2.0.co;2

Allmendinger, R. W., Nelson, K. D., Potter, C. J., Barazangi, M., Brown, L. D., & Oliver, J. E. (1987b). Deep seismic reflection characteristics of the continental crust. *Geology*, 15(4), 304–310. https://doi.org/10.1130/0091-7613(1987)15<304:dsrcot>2.0.co;2

Allmendinger, R. W., Sharp, J. W., Von Tish, D., Serpa, L., Brown, L., Kaufman, S., et al. (1983). Cenozoic and Mesozoic structure of the eastern Basin and Range province, Utah, from COCORP seismic-reflection data. *Geology*, 11(9), 532–536. https://doi.org/10.1130/0091-7613(1983) 11<532:camsot>2.0 co:2

Anders, M. H., Geissman, J. W., Piety, L. A., & Sullivan, J. T. (1989). Parabolic distribution of circumeastern Snake River Plain seismicity and latest Quaternary faulting: Migratory pattern and association with the Yellowstone hotspot. *Journal of Geophysical Research*, 94(B2), 1589–1621. https://doi.org/10.1029/jb094jb02p01589

Anders, M. H., & Sleep, N. H. (1992). Magmatism and extension: The thermal and mechanical effects of the Yellowstone hotspot. *Journal of Geophysical Research*, 97(B11), 15379–15393. https://doi.org/10.1029/92jb01376

Barnosky, A. D. (1984). The Colter Formation: Evidence for Miocene volcanism in Jackson Hole, Teton County, Wyoming. *Earth Science Bulletin*, 17, 49–97.

Beaumont, C. (1979). On rheological zonation of the lithosphere during flexure. *Tectonophysics*, 59(1–4), 347–365. https://doi.org/10.1016/0040-1951(79)90055-6

Behrendt, J. C., Tibbetts, B. L., Bonini, W. E., Lavin, P. M., Love, J. D., & Reed, J. C., Jr. (1968). A geophysical study in Grand Teton National Park and vicinity, Teton County, Wyoming, with sections on stratigraphy and structure and Precambrian rocks. U.S. Geological Survey Professional Paper, 516-E.

Blackstone, D. L., Jr. (1993). Precambrian basement map of Wyoming – Outcrop and structural configuration: Wyoming State Geological Survey Map Series 43, scale 1:1,000,000.

Blackwelder, E. (1915). Post-Cretaceous history of the mountains of central western Wyoming. The Journal of Geology, 23(4), 193–217. https://doi.org/10.1086/622243

Blackwell, D. D., & Richards, M. C. (2004). The 2004 geothermal map north America: Explanation of resources and applications (Vol. 28, pp. 317–320). Geothermal Resources Council Transactions.

Braun, J. (2002). Quantifying the effect of recent relief changes on age–elevation relationships. *Earth and Planetary Science Letters*, 200(3–4), 331–343. https://doi.org/10.1016/s0012-821x(02)00638-6

Braun, J. (2003). Pecube: A new finite-element code to solve the 3D heat transport equation including the effects of a time-varying, finite amplitude surface topography. *Computers & Geosciences*, 29(6), 787–794. https://doi.org/10.1016/s0098-3004(03)00052-9

Braun, J., Van Der Beek, P., Valla, P., Robert, X., Herman, F., Glotzbach, C., et al. (2012). Quantifying rates of landscape evolution and tectonic processes by thermochronology and numerical modeling of crustal heat transport using PECUBE. *Tectonophysics*, 524–525, 1–28. https://doi.org/10.1016/j.tecto.2011.12.035

Brown, L. D., Wille, D., Zheng, L., DeVoogd, B., Mayer, J., Hearn, T., et al. (1987). COCORP: New perspectives on the deep crust. *Geophysical Journal International*, 89(1), 47–54. https://doi.org/10.1111/j.1365-246X.1987.tb04386.x

Brown, S. J., Thigpen, J. R., Spotila, J. A., Krugh, W. C., Tranel, L. M., & Orme, D. A. (2017). Onset timing and slip history of the Teton fault, Wyoming: A multidisciplinary evaluation [Dataset]. *Tectonics*, 36(11), 2669–2692. https://doi.org/10.1002/2016TC004462

Byrd, J. O. D., & Smith, R. B. (1990). Dating recent faulting and estimates of slip rates for the southern segment of the Teton fault, Wyoming. *Geological Society of America Abstracts with Programs*, 22(6), 4–5.

Byrd, J. O. D., Smith, R. B., & Geissman, J. W. (1994). The Teton fault, Wyoming: Topographic signature, neotectonics, and mechanisms of deformation. *Journal of Geophysical Research*, 99(B10), 20095–20122. https://doi.org/10.1029/94JB00281

Chávez-Pérez, S., Louie, J. N., & Pullammanappallil, S. K. (1998). Seismic depth imaging of normal faulting in the southern Death Valley basin. *Geophysics*, 63(1), 223–230. https://doi.org/10.1190/1.1444316

Christiansen, R. L., Blank, H. R., Jr., Love, J. D., & Reed, J. C., Jr. (1978). Geologic map of the Grassy Lake Reservoir Quadrangle, Yellowstone National Park and vicinity, Wyoming, scale 1:62,500. U.S. Geological Survey Quadrangle Map GQ-1459.

Christiansen, R. L., Blank, H. R., Love, J. D., Jr., & Reed, J. C., Jr. (1978). Geologic map of the Grassy Lake Reservoir Quadrangle, Yellowstone National Park and Vicinity, Wyoming. U.S. Geological Survey Open-File Report GQ-1459.

Colgan, J. P., Dumitru, T. A., Reiners, P. W., Wooden, J. L., & Miller, E. L. (2006). Cenozoic tectonic evolution of the Basin and Range province in northwestern Nevada. American Journal of Science, 306(8), 616–654. https://doi.org/10.2475/08.2006.02

HELFRICH ET AL. 26 of 29



- Colgan, J. P., Shuster, D. L., & Reiners, P. W. (2008). Two-phase Neogene extension in the northwestern Basin and Range recorded in a single thermochronology sample. Geology, 36(8), 631–634. https://doi.org/10.1130/G24897A.1
- Curry, M. A. E., Barnes, J. B., & Colgan, J. P. (2016). Testing fault growth models with low temperature thermochronology in the northwest Basin and Range, USA. *Tectonics*, 35(10), 2467–2492. https://doi.org/10.1002/2016TC004211
- Densmore, A. L., Dawers, N. H., Gupta, S., Guidon, R., & Goldin, T. (2004). Footwall topographic development during continental extension. *Journal of Geophysical Research*, 109(F3), F03001. https://doi.org/10.1029/2003JF000115
- Dirks, R. A. (1982). The climate of Yellowstone and Grand Teton National Parks, US Department of the Interior. National Park Service Occasional Paper, no. 6 (pp. 1–26).
- DuRoss, C. B., Gold, R. D., Briggs, R. W., Delano, J. E., Ostenaa, D. A., Zellman, M. S., et al. (2019). Holocene earthquake history and slip rate of the southern Teton fault, Wyoming, USA. Geological Society of America Bulletin, 132(7–8), 1566–1586. https://doi.org/10.1130/B35363.1
- DuRoss, C. B., Zellman, M. S., Thackray, G. D., Briggs, R. W., Gold, R. D., & Mahan, S. A. (2021). Holocene paleoseismology of the Steamboat Mountain Site: Evidence for full-length rupture of the Teton Fault, Wyoming. Bulletin of the Seismological Society of America, 111(1), 439– 465. https://doi.org/10.1785/0120200212
- Edmund, R. W. (1951). Structural geology and physiography of the northern end of the Teton Range, Wyoming (Vol. 23, p. 81). Augustana Library Publication.
- Egan, S. S., Buddin, T. S., Kane, S. J., & Williams, G. D., (1997). Three-dimensional modelling and visualization in structural geology: New techniques for the restoration and balancing of volumes. In *Proceedings of the 1996 geoscience 144 information group conference on geological visualization: Electronic geology special* (Vol. 1, pp. 67–82).
- Ehlers, T. A. (2005). Crustal thermal processes and the interpretation of thermochronometer data. *Reviews in Mineralogy and Geochemistry*, 58(1), 315–350. https://doi.org/10.2138/rmg.2005.58.12
- Ehlers, T. A. (2023). Pecube-D: Thermokinematic and erosion modeling software for problems in tectonics and surface processes [Software]. Zenodo. https://doi.org/10.5281/zenodo.7785668
- Ehlers, T. A., & Farley, K. A. (2003). Apatite (U-Th)/He thermochronometry: Methods and applications to problems in tectonic and surface processes. *Earth and Planetary Science Letters*, 206(1–2), 1–14. https://doi.org/10.1016/s0012-821x(02)01069-5
- Ehlers, T. A., Willett, S. D., Armstrong, P. A., & Chapman, D. S. (2003). Exhumation of the central Wasatch Mountains, Utah: 2. Thermokinematic model of exhumation, erosion, and thermochronometer interpretation. *Journal of Geophysical Research*, 108(B3). https://doi.org/10.1029/2001JB001723
- Foster, D., Brockelhurst, S. H., & Gawthorpe, R. L. (2010). Glacial-topographic interactions in the Teton Range, Wyoming. *Journal of Geophysical Research*, 115(F1). https://doi.org/10.1029/2008JF001135
- Fryxell, F. M., Horberg, L., & Edmund, R. (1941). Geomorphology of the Teton Range and adjacent basins. *Geological Society of America Bulletin*, 49, 1903.
- Galadini, F., & Galli, P. (2000). Active tectonics in the Central Apennines (Italy) Input data for seismic hazard assessment. *Natural Hazards*, 22(3), 225–268. https://doi.org/10.1023/A:1008149531980
- Gallagher, K. (2012). Transdimensional inverse thermal history modelling for quantitative thermochronology. *Journal of Geophysical Research*, 117(B2), B02408. https://doi.org/10.1029/2011JB008825
- Gilbert, J. D., Ostenaa, D., & Wood, C. (1983). Seismotectonic study of Jackson Lake Dam and Reservoir, Minidoka Project, Idaho-Wyoming (Vol. 83-8, p. 123). Bureau of Reclamation Seismotectonic Report.
- Green, P. F., Duddy, I. R., Laslett, G. M., Hegarty, K. A., Gleadow, J. W., & Lovering, J. F. (1989). Thermal annealing of fission tracks in apatite:
 4. Quantitative modeling techniques and extension to geological timescales. *Chemical Geology*, 79, 155–195.
- Heasler, H. P. (1987). Geothermal modeling of Jackson Hole, Teton County Wyoming. Technical Report for the Department of Energy, NTIS Issue No. 198723 (p. 38).
- Helfrich, A. L. (2020). Testing interpretations of the displacement magnitude of the Teton fault and uplift of the Teton Range, Wyoming with integrated flexural-kinematic and thermal modeling [M.S. thesis] (p. 157). University of Kentucky. https://doi.org/10.13023/etd.2020.487
- Horberg, L., Nelson, V., & Church, V. (1949). Structural trends in central-western Wyoming. Geological Society of America Bulletin, 60(1), 183–216. https://doi.org/10.1130/0016-7606(1949)60[183:sticww]2.0.co;2
- Kane, S. J., Williams, G. D., Buddin, T. S., Egan, S. S., & Hodgetts, D. (1997). Flexural-slip based restoration in 3-D; A new approach. AAPG Search and Discovery #91021.
- Ketcham, R. A., Carter, A., Donelick, R. A., Barbarand, J., & Hurford, A. J. (2007). Improved modeling of fission-track annealing in apatite. American Mineralogist, 92(5–6), 799–810. https://doi.org/10.2138/am.2007.2281
- Ketcham, R. A., Donelick, R. A., & Carlson, W. D. (1999). Variability of apatite fission-track annealing kinetics: III. Extrapolation to geological time scales. American Mineralogist, 84(9), 1235–1255. https://doi.org/10.2138/am-1999-0903
- Lageson, D. R. (1992). Possible Laramide influence on the Teton normal fault, western Wyoming. In P. K. Link, M. A. Kuntz, & L. B. Platt (Eds.), Regional geology of eastern Idaho and western Wyoming (Vol. 179, pp. 183–195). Geological Society of America Memoir.
- Larsen, D. J., Crump, S. E., Abbott, M. B., Harbert, W., Blumm, A., Wattrus, N. J., & Hebberger, J. J. (2019). Paleoseismic evidence for climatic and magmatic controls on Teton Fault. Geophysical Research Letters, 46(22), 13036–13043. https://doi.org/10.1029/2019GL085475
- Laslett, G. M., Galbraith, R. F., & Green, P. F. (1994). The analysis of projected fission track lengths. *Radiation Measurements*, 23(1), 103–123. https://doi.org/10.1016/1350-4487(94)90028-0
- Lavin, P. M., & Bonini, W. E. (1957). Detailed gravity measurements in the Teton Range and Jackson Hole, Wyoming. Geological Society of America Bulletin, 68, 1760.
- Long, S. P. (2019). Geometry and magnitude of extension in the Basin and Range Province (39°N), Utah, Nevada, and California, USA: Constraints from a province-scale cross section. GSA Bulletin, 131(1-2), 99-119. https://doi.org/10.1130/B31974.1
- Love, J. D. (1977). Summary of Upper Cretaceous and Cenozoic stratigraphy, and of tectonic and glacial events in Jackson Hole, northwestern Wyoming. In Wyoming geological association guidebook, 29th annual field conference (pp. 586–593).
- Love, J. D. (1987). Teton mountain front, Wyoming. In S. S. Beus (Ed.), Rocky Mountain section of the geological society of America DNAG centennial field guide (Vol. 2, pp. 173–178). https://doi.org/10.1130/0-8137-5402-X
- Love, J. D. (2004). Geologic map of the Moran quadrangle, Teton County, Wyoming. Wyoming State Geological Survey Map LMS-11.
- Love, J. D., & Albee, H. F. (1972). Geologic map of the Jackson Quadrangle, Teton County, Wyoming. U.S. Geological Survey, Miscellaneous Geologic Investigations Map I-769-A, scale 1:24,000.
- Love, J. D., Leopold, E. B., & Love, D. W. (1978). Eocene rocks, fossils, and geologic history, Teton, northwestern Wyoming. U.S. Geological Survey Professional Paper, 932-B. In J. D. Love (Ed.), Geology of the Teton-Jackson Hole region, northwestern Wyoming (pp. B1–B40).
- Love, J. D., & Love, C. M. (2000). Geologic map of the Cache Creek quadrangle, Teton County, Wyoming. Geological Survey of Wyoming J.D. Series Map LMS-1, scale 1:24,000.

HELFRICH ET AL. 27 of 29



- Love, J. D., & Reed, J. C. (1971). Creation of the Teton landscape: Grand Teton Natural History Association, Moose, Wyoming (p. 120).
- Love, J. D., & Reed, J. C., Jr. (1975). Geologic map of the Teton Village quadrangle, Teton County, Wyoming. U.S. Geological Survey Open-File Report 75-335, scale 1:24,000.
- Love, J. D., & Reed, J. C., Jr. (2000). Geologic map of the Teton Village quadrangle, Teton County, Wyoming. Geological Survey of Wyoming J. D. Love Series Map LMS-2, scale 1:24,000.
- Love, J. D., Reed, J. C., Jr., & Christiansen, A. C. (1992). Geologic Map of Grand Teton National Park, Teton County, Wyoming. U.S. Geological Survey Miscellaneous Investigations Series, I-2031, scale 1:62,500.
- Lowry, A. R., & Smith, R. B. (1994). Flexural rigidity of the Basin and Range-Colorado Plateau-Rocky Mountain transition from coherence analysis of gravity and topography. *Journal of Geophysical Research*, 99(B10), 20123–20140. https://doi.org/10.1029/94JB00960
- Lowry, A. R., & Smith, R. B. (1995). Strength and rheology of the western U.S. Cordillera. *Journal of Geophysical Research*, 100(B9), 17947–17963. https://doi.org/10.1029/95JB00747
- Masbruch, M. D., Chapman, D. S., & Solomon, D. K. (2012). Air, ground, and groundwater recharge temperatures in an alpine setting, Brighton Basin, Utah. Water Resources Research, 48(10). https://doi.org/10.1029/2012wr012100
- McQuarrie, N., & Ehlers, T. A. (2015). Influence of thrust belt geometry and shortening rate on thermochronometer cooling ages: Insights from thermokinematic and erosion modeling of the Bhutan Himalaya. *Tectonics*, 34(6), 1055–1079. https://doi.org/10.1002/2014TC003783
- McQuarrie, N., & Ehlers, T. A. (2017). Techniques for understanding fold-and-thrust belt kinematics and thermal evolution. In R. D. Law, J. R. Thigpen, A. J. Merschat, & H. H. Stowell (Eds.), Linkages and feedbacks in orogenic systems (Vol. 213, pp. 25–54). Geological Society of America Memoir, https://doi.org/10.1130/2017.1213(02)
- McQuarrie, N., & Rodgers, D. W. (1998). Subsidence of a volcanic basin by flexure and lower crustal flow: The eastern Snake River Plain, Idaho. *Tectonics*, 17(2), 203–220. https://doi.org/10.1029/97tc03762
- Mohapatra, G. K., & Johnson, R. A. (1998). Localization of listric faults at thrust fault ramps beneath the Great Salt Lake Basin, Utah: Evidence from seismic imaging and finite element modeling. *Journal of Geophysical Research*, 103(B5), 10047–10063. https://doi.org/10.1029/98ib00023
- Ortner, H., Sanders, D., & Pomella, H. (2022). Long-term morpho-structural development of major normal fault zones, Gran Sasso area, Central Apennines (Italy). *Geomorphology*, 413, 108350. https://doi.org/10.1016/j.geomorph.2022.108350
- Pérez-Peña, J. V., Al-Awabdeh, M., Azañón, J. M., Galve, J. P., Booth-Rea, G., & Notti, D. (2017). Swathprofiler and NProfiler: Two new ArcGIS Add-ins for the automatic extraction of swath and normalized river profiles. Computers & Geosciences, 104, 135–150. https://doi.org/10.1016/j.cageo.2016.08.008
- Pierce, K. L., Licciardi, J. M., Good, J. M., & Jaworoski, C. (2018). Pleistocene glaciation of the Jackson Hole area, Wyoming. U.S. Geological Survey Professional Paper 1835 (p. 56). https://doi.org/10.3133/pp1835
- Pierce, K. L., & Morgan, L. A. (1990). The track of the Yellowstone hotspot: Volcanism, faulting, and uplift (Vols. 90–145, p. 49). U.S. Geological Survey Open-File Report
- Pierce, K. L., & Morgan, L. A. (1992). The track of the Yellowstone hot spot: Volcanism, faulting, and uplift. In P. K. Link, M. A. Kuntz, & L. B. Platt (Eds.), Regional geology of eastern Idaho and western Wyoming (Vol. 179, pp. 1–53). Geological Society of America Memoir.
- Pierce, K. L., & Morgan, L. A. (2009). Is the track of the Yellowstone hotspot driven by a deep mantle plume? Review of volcanism, faulting, and uplift in light of new data. *Journal of Volcanology and Geothermal Research*, 188(1–3), 1–25. https://doi.org/10.1016/j.jvolgeores.2009.07.009
- Rahn, M. K., & Grasemann, B. (1999). Fission track and numerical thermal modeling of differential exhumation of the Glarus thrust plane (Switzerland). Earth and Planetary Science Letters, 169(3-4), 245-259. https://doi.org/10.1016/s0012-821x(99)00078-3
- Reed, J. C., Jr. (1973). Geologic map of the Precambrian rocks of the Teton Range, Wyoming. U.S. Geological Survey Open-File Report, scale 1:62,500.
- Roberts, S. V., & Burbank, D. W. (1993). Uplift and thermal history of the Teton Range (northwestern Wyoming) defined by apatite fission-track dating. Earth and Planetary Science Letters, 118(1–4), 295–309. https://doi.org/10.1016/0012-821x(93)90174-8
- Rodgers, D. W., Ore, H. T., Bobo, R. T., McQuarrie, N., & Zentner, N. (2002). Extension and subsidence of the eastern Snake River Plain, Idaho. In B. Bonnichsen, C. M. White, & M. McCurry (Eds.), *Tectonic and magmatic evolution of the Snake River Plain Volcanic Province* (Vol. 30, pp. 121–155). Idaho Geological Survey Bulletin.
- Smith, R. B., & Bruhn, R. L. (1984). Intraplate extensional tectonics of the eastern Basin and Range: Inferences on structural style from seismic reflection data, regional tectonics, and thermal-mechanical models of brittle-ductile deformation. *Journal of Geophysical Research*, 89(B7), 5733–5762. https://doi.org/10.1029/ib089ib07p05733
- Smith, R. B., Byrd, J. O. D., Bruhn, R. L., Susong, D. D., & Sylvester, A. G. (1990). An evaluation of earthquake hazards of the Grand Teton National Park Emphasizing the Teton Fault (Vol. 14). University of Wyoming National Park Service Research Center Annual Report.
- Smith, R. B., Byrd, J. O. D., & Susong, D. D. (1993). The Teton fault, Wyoming: Seismotectonics, Quaternary history, and earthquake hazards. In A. W. Snoke, J. R. Steidtmann, & S. M. Roberts (Eds.), Geology of Wyoming: Geological survey of Wyoming Memoir (Vol. 5, pp. 628–667).
- Smith, R. B., & Sbar, M. L. (1974). Contemporary tectonics and seismicity of the western United States with emphasis on the Intermountain Seismic Belt. Geological Society of America Bulletin, 85(8), 1205–1218. https://doi.org/10.1130/0016-7606(1974)85<1205:ctasot>2.0.co;2
- Stockli, D. F., Dumitru, T. A., McWilliams, M. O., & Farley, K. A. (2003). Cenozoic tectonic evolution of the White Mountains, California and Nevada. Geological Society of America Bulletin, 115(7), 788–816. https://doi.org/10.1130/0016-7606(2003)115
- Stockli, D. F., Surpless, B. E., Dumitru, T. A., & Farley, K. A. (2002). Thermochronological constraints on the timing and magnitude of Pliocene extension in the central Wassuk Range, western Nevada. *Tectonics*, 21(4). https://doi.org/10.1029/2001TC001295
- Stüwe, K., White, L., & Brown, R. (1994). The influence of eroding topography on steady-state isotherms: Application to fission track analysis. Earth and Planetary Science Letters, 124(1-4), 63–74. https://doi.org/10.1016/0012-821x(94)00068-9
- Tesauro, M., Kaban, M. K., & Mooney, W. D. (2015). Variations of the lithospheric strength and elastic thickness in North America. Geochemistry, Geophysics, Geosystems, 16(7), 2197–2220. https://doi.org/10.1002/2015gc005937
- Thackray, G. D., & Staley, A. E. (2017). Systematic variation of Late Pleistocene fault scarp height in the Teton Range, Wyoming, USA: Variable fault slip rates or variable landform ages? *Geosphere*, 13(2), 287–300. https://doi.org/10.1130/GES01320.1
- Thigpen, J. R., Brown, S. J., Helfrich, A. L., Hoar, R. M., McGlue, M. M., Woolery, E. W., et al. (2021). Removal of the northern paleo-Teton Range along the Yellowstone hotspot track [Dataset]. *Lithosphere*, 2021(1). https://doi.org/10.2113/2021/1052819
- Thompson, G. A., & Parsons, T. (2009). Can footwall unloading explain late Cenozoic uplift of the Sierra Nevada crest? *International Geology Review*, 51(9–11), 986–993. https://doi.org/10.1080/00206810903059156
- Tibbetts, B. L., Behrendt, J. C., & Love, J. D. (1969). Seismic refraction measurements in Jackson Hole, Wyoming. Geological Society of America Bulletin, 80(6), 1109–1122. https://doi.org/10.1130/0016-7606(1969)80[1109:smijhw]2.0.co;2
- Touloukian, Y. S., Judd, W. R., & Roy, R. F. (Eds.). (1989). Physical properties of rocks and minerals. CINDAS data series on material properties, Group II, Properties of special materials, II-2. McGraw-Hill.

HELFRICH ET AL. 28 of 29



- Turcotte, D. L. (1979). Flexure. Advances in Geophysics, 21, 51-86. https://doi.org/10.1016/s0065-2687(08)60261-7
- Turcotte, D. L., & Schubert, G. (2002). Geodynamics (2nd ed.). Cambridge University Press.
- Velasco, M. S., Bennett, R. A., Johnson, R. A., & Hreinsdóttir, S. (2010). Subsurface fault geometries and crustal extension in the eastern Basin and Range province, western U.S. *Tectonophysics*, 488(1–4), 131–142. https://doi.org/10.1016/j.tecto.2009.05.010
- Von Tish, D. B., Allmendinger, R. W., & Sharp, J. W. (1985). History of Cenozoic extension in central Sevier Desert, west-central Utah, from COCORP seismic reflection data. AAPG Bulletin, 69, 1077–1087. https://doi.org/10.1306/ad462b7d-16f7-11d7-8645000102c1865d
- Walcott, R. I. (1970). Flexural rigidity, thickness, and viscosity of the lithosphere. Journal of Geophysical Research, 75, 3941–3954. https://doi.org/10.1002/9781118782149.ch16
- Watts, A. B. (2001). Isostasy and flexure of the lithosphere (p. 508). Cambridge University Press.
- Watts, A. B., & Burov, E. B. (2003). Lithospheric strength and its relationship to the elastic and seismogenic layer thickness. *Earth and Planetary Science Letters*, 213(1–2), 113–131. https://doi.org/10.1016/s0012-821x(03)00289-9
- Watts, A. B., Karner, G., & Steckler, M. S. (1982). Lithospheric flexure and the evolution of sedimentary basins. *Philosophical Transactions of the Royal Society of London Series A: Mathematical and Physical Sciences*, 305, 249–281.
- Wernicke, B. (1981). Low-angle normal faults in the Basin and Range Province: Nappe tectonics in an extending orogen. *Nature*, 291(5817), 645–648. https://doi.org/10.1038/291645a0
- Wernicke, B., & Burchfiel, B. C. (1982). Modes of extensional tectonics. *Journal of Structural Geology*, 4(2), 105–115. https://doi.org/10.1016/0191-8141(82)90021-9
- White, B. J. P., Smith, R. B., Husen, S., Farrell, J. M., & Wong, I. (2009). Seismicity and earthquake hazard analysis of the Teton-Yellowstone region, Wyoming. *Journal of Volcanology and Geothermal Research*, 188(1–3), 277–296. https://doi.org/10.1016/S0022-3115(97)00271-7
- Wyoming State Geological Survey. (2022). Precambrian basement map of Wyoming: Structural configuration. Wyoming State Geological Survey Open File Report 2022-5 (p. 8). scale 1:500,000.
- Zellman, M. S., DuRoss, C. B., & Thackray, G. D. (2019a). The Teton Fault, Teton County, Wyoming. Wyoming Geological Survey Open File Report 2019-1.
- Zellman, M. S., DuRoss, C. B., Thackray, G. D., Briggs, R. W., Cholewinski, N., Reyes, T., et al. (2018). A paleoseismic investigation of the northern Teton fault at the Steamboat Mountain Trench Site, Grand Teton National Park, Wyoming. Seismological Research Letter, 89, 837.
- Zellman, M. S., DuRoss, C. B., Thackray, G. D., Personius, S. F., Reitman, N. G., Mahan, S. A., & Brossy, C. C. (2019b). Holocene rupture history of the Central Teton Fault at Leigh Lake, Grand Teton National Park, Wyoming. *Bulletin of the Seismological Society of America*, 110(1), 67–82. https://doi.org/10.1785/0120190129

HELFRICH ET AL. 29 of 29